

Abundances of Elements in Exoplanet Host Stars

Vasco de Matos Ferreira Mendes Neves

Department of Physics - University of Aveiro (DFUA)
Centro de Astrofísica da Universidade do Porto (CAUP)

Orientation by:
Alexandre Correia (UA)
Nuno Santos (CAUP)

June of 2008

Contents

1	Introduction	1
	Introduction	1
1.1	In the Beginning...	1
1.2	The Radial Velocity Technique	2
1.3	The Photometric Transit Technique	3
1.4	Astrometry	4
1.5	Microlensing	5
1.6	A Statistical 'Zoo' of Exoplanets	6
1.7	The Formation of Planetary Systems	7
1.8	The Host Star Chemical Properties	8
1.8.1	The Metallicity Distribution	8
1.8.2	Abundance of other Elements	10
1.8.3	Correlations between Metallicity and Orbital Parameters	11
1.9	Our Work	11
2	Determination of the Chemical Abundances	12
2.1	Introduction	12
2.2	Local Thermodynamic Equilibrium	12
2.3	The Behaviour of Line Strength	14
2.3.1	The Measurement of the EW	14
2.3.2	The Abundance Dependence	15
2.3.3	The Temperature Dependence	15
2.3.4	The Pressure Dependence	17
2.3.5	Microturbulence and Velocity Fields	18
2.4	Calculation of the Abundance	18
2.4.1	Differential Analysis	19
3	Data and Spectral Analysis	20
3.1	The HARPS Spectrograph	20

3.2	Spectral Data	20
3.3	Identification and Selection of the Spectral Lines	22
3.3.1	Using VALD to Obtain the Initial List of Spectral Lines	23
3.3.2	Using IRAF to Identify the 'Good' Lines	23
3.3.3	Measuring the EWs of the Solar Lines with ARES	24
3.3.4	Calculating New Oscillator Strengths	25
3.3.5	A Test using the Solar Abundance Values	25
3.3.6	The Molecular Equilibrium	26
3.3.7	Testing a small sub-sample Containing 20 Stars	26
3.4	Spectral Analysis of the Full Sample	28
3.4.1	Uncertainties	29
3.4.2	Testing the Stellar Parameters and Searching for Systematic Effects	30
4	Results: the Abundance of Stars with Planets	36
4.1	Comparison of $[X/H]$ Values with the Literature	36
4.2	The $[X/H]$ Distributions	38
4.3	The $[X/Fe]$ versus $[Fe/H]$ Plots	40
4.3.1	Metallicity Anomalies in Planet Host Stars	43
5	Conclusions and Future Work	45
5.1	Conclusions	45
5.2	Future Work	46
	Bibliography	47

Chapter 1

Introduction

1.1 In the Beginning...

Since immemorial times man has asked himself if he was alone in the Universe. If there was life elsewhere beyond Earth. If there were places out there where sentient beings could live and wonder about the same questions...who are we? where do we came from? where are we going...?

When the first exoplanet around a solar type star, 51 Peg b, was discovered, by Mayor & Queloz (1995), a first, tiny piece of the huge puzzle that could answer these ages old questions was put into place. This discovery turned out to be one of the biggest breakthroughs in astrophysics of all times and sent shock waves that rippled through the teeming masses of humanity: there are other planetary systems in the Universe beyond our own...what next?

Although this discovery and the others that followed shortly (e.g. Marcy & Butler 1996) had only detected giant planets with masses of the order of magnitude of Jupiter, the seed of possibilities had already been casted and the impact of these discoveries not only opened a new field in astrophysics but also the minds and imagination of everyone. They have inspired passionate debates and, suddenly, old questions arrived renewed. Are there other Earths orbiting other stars? Is life exclusive to Earth or is it common throughout the galaxy and the universe? Does this life, if it really exists, evolved and gained intelligence? And so on.

Unfortunately, it does take endless hours of painstaking research and perseverance to reach for even the smallest answer. And then many more questions follow...that's how Science works! But let us now change subjects and move on to more practical questions: the techniques that allowed the discovery of the exoplanet systems around solar type stars and their characterisation.

1.2 The Radial Velocity Technique

Those first discoveries, and most of the exoplanets found nowadays ($\sim 94\%$), are based in the radial velocity (RV) technique. The use of this technique to detect planetary bodies was first proposed by Struve (1952). It consists in the detection of the Doppler shift produced in the star's spectrum by the subtle 'wobbling' of the star due to the presence of a planet in its orbit. If the star is moving toward Earth its light will be shifted to the 'blue' (i.e. the spectral lines will move to shorter wavelengths). However, if the star is moving away from Earth its light will be red-shifted (i.e. the lines will move to longer wavelengths). This is illustrated in Fig. 1.1a. The radial velocity of the star can then be deduced from the displacement of the spectral lines. In Fig. 1.1b we can see such variation depicting the orbital motion of a star.

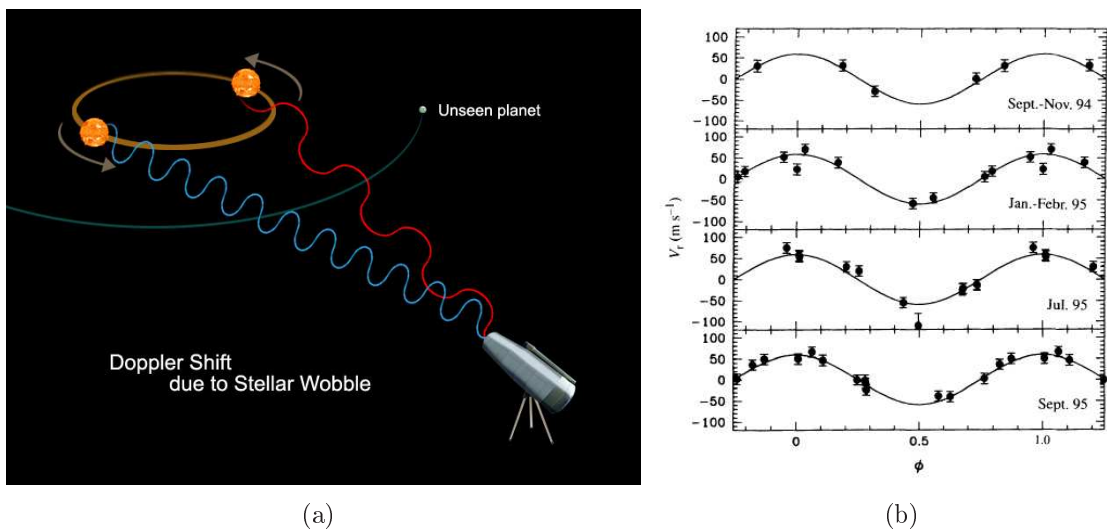


Figure 1.1: a) Illustration showing how the radial velocity technique works. Credits: www.nasa.gov; b) Plots of radial velocity as function of the orbital phase, showing the orbital motion of 51 Peg at four different epochs (Mayor & Queloz 1995).

With the RV technique we can only ascertain with relative precision some orbital parameters (the semi major axis of the planet's orbit, eccentricity and orbital period) and a lower limit of the planet's mass. We cannot obtain the exact value of the mass because we lack the value of the planet's orbit inclination to the line perpendicular to the line of sight. This fact is clearly expressed by the so called mass function,

$$f(m) = \frac{(m \sin i)^3}{(M + m)^2} = 1.036 \times 10^{-7} K^2 (1 - e)^{3/2} P \quad [M_\odot] \quad (1.1)$$

where m and M is the planet and star mass, respectively, both expressed in solar masses, i the inclination, e the eccentricity, K the measured semi-amplitude of the radial velocity, given in km/s , and P the measured period of the star's wobble (that

is equal to the planet's orbital period around the star), given in days. The P , e and K can be directly obtained from the RV curve. The $m \sin i$ is then calculated with this equation. For a detailed demonstration refer to Santos (2008). From Eq. (1.1) we can clearly see that the amplitude of the radial velocity will be greater if the planet is closer and/or is more massive. This means that planets with smaller masses and further away from the star will be more difficult to detect.

The RV technique does not give us the attributes for the planet radius and is unsuitable to detect planets in stars that are too massive, instable or rotate too rapidly. Therefore, the detection of planets with it is restricted to 'quiet' FGKM dwarf stars. If we want to acquire the radius and, with it, the mean density of the planet, we need to use other techniques such as photometric transits or astrometry and combine the data of the two methods.

Nevertheless, the RV technique is far from having reached its highest point: It is expected that the precision can reach a limit of 1 cm/s, enabling the detection of sub Earth planets (Lovis et al. 2006).

1.3 The Photometric Transit Technique

A photometric transit occurs when a planet crosses in front of its host star and blocks part of its light. The photometric transit technique consists in the measurement of the variation of the star's brightness at the moment of the transit. For a Jupiter like planet, the brightness of the star is reduced by $\sim 1\%$ and for less massive planets the variation is even smaller (Santos 2008).

This technique can only detect orbits of planets closely aligned with Earth. The estimated probability that a full transit will happen is given by the geometric probability, $P = R_{star}/a$, where R_{star} and a are the stellar and orbital radius, respectively. This formula is an approximation and is only valid for near-circular orbits. While the probability of detecting a planet with an orbital period of 3 days is about 10%, it goes down to 0.5% for a planet orbiting 1 AU¹ from its star.

Another disadvantage relates to its high rate of false detections, where changes in the brightness of the star are induced by other phenomena such as eclipsing binaries, grazing stellar eclipses or variations in the chromospheric activity. Therefore, the only way to be sure that a positive detection was achieved is to do a follow up with RV.

The greatest advantage of the transit technique is that we can determine the radius of the planet from the light-curve. We can see an example of a phototransit event in Fig. 1.2.

¹Astronomical Unit

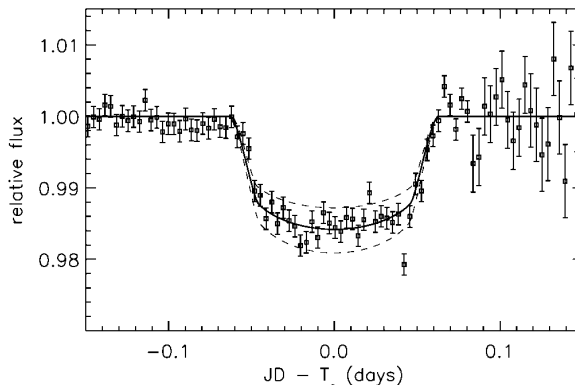


Figure 1.2: Photometric time series, binned into 5 minute averages. The solid line represents the best fit for data. The dashed lines represent transit curves if the transit planet had $\pm 10\%$ in size. From Charbonneau et al. (2000).

Unfortunately, we cannot acquire the mass of the planet with this technique alone. However, if we combine the information obtained in RV with the one obtained in a photometric transit (Charbonneau et al. 2000), we can determine the exact mass and the mean density of the planet.

The future of the transit technique is most promising: today, dozens of surveys are made and the possibility to study the density and atmospheric composition of the planets is within reach. Higher expectations came from the space based missions, both present (CoRoT) and future (Kepler): they may allow the detection of Earth size or even smaller planets. In conjunction with RV it will be possible to study the 'Earth domain' mass-radius relation.

1.4 Astrometry

Astrometry is the oldest searching method for detecting extrasolar planets but not the most effective (yet). It consists in the very precise measuring of a star's position against the background over time. The presence of another sufficiently orbiting massive body will make the detection of the star's motion around the centre of mass of the system possible. The first confirmation of an exoplanet with this method was made by Benedict et al. (2002), using the Hubble Space Telescope (HST).

Unfortunately, current astrometric technology does not allow the detection of planetary bodies from scratch: up to now, all detections made with astrometry were follow-ups to successful measurements with RV. It will be needed to surpass the 1 micro-arc-second threshold for an independent and reliable detection of planetary bodies with astrometry.

In conjunction with RV, it gives the exact mass of the planet, along with astrometric parameters (perturbation of the semimajor axis, inclination and absolute parallax).

Astrometry is also complementary of RV in the sense that it is more sensitive to longer period planets. On the top of that, it enables the detection of companions in stars where RV is impracticable: A,B stars and T-Tauri stars.

Regarding astrometry, the space missions HST and the James Webb Space Telescope and the ground-based mission Very Large Telescope Interferometer will enable the gathering of astrometric parameters from planetary systems and allow the determination of the exact mass of the planetary companions. Further in the future, the space missions GAIA and SIM will, hopefully, detect thousands of planets by pushing the detection limits toward sub Earth mass planets.

1.5 Microlensing

In this context we should not forget the role of a promising technique, microlensing (Beaulieu et al. 2006), also very complementary of RV, with the potential of detecting sub earth mass bodies in long period orbits. Microlensing occurs when the gravitational field of a star acts like a lens, magnifying the light from distant stars. If the star that provokes the lensing has a planet, then the planet's field might make a detectable contribution. One example can be seen in Fig. 1.3.

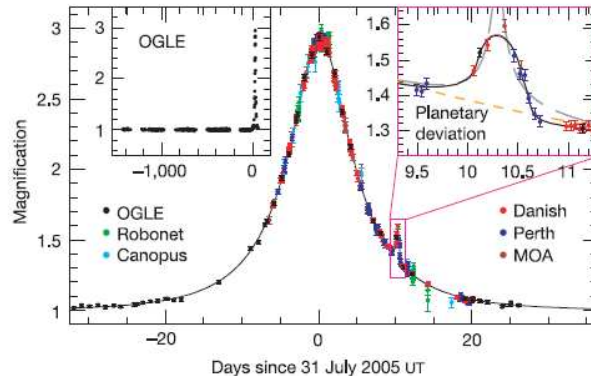


Figure 1.3: Observed light curve of the OGLE-2005-BLG-390 microlensing event and best-fit model plotted as a function of time. From Beaulieu et al. (2006).

We can estimate the mass, period and semimajor axis of the planet with this method. However, it has a great disadvantage: the lensing is difficult to reproduce because the chance alignment may never occur again. Moreover, the detected planets need to be far away from us, typically in the galactic bulge, which makes follow up by other methods impossible with the present technology (i.e. RV, Astrometry).

All methods of planetary detection, present and future, along with future ground and space based missions can be reviewed in Perryman et al. (2005).

1.6 A Statistical 'Zoo' of Exoplanets

Up to now, and according to 'The Extrasolar Planets Encyclopaedia'², there are 289 planet candidates detected in 252 planetary systems³. The system with the greatest number of planetary bodies found is 55 Cancri, with 5 planets (Fischer et al. 2008) and the smallest planet yet discovered is MOA-2007-BLG-192-Lb (Bennett et al. 2008) with a mass around 3.3 Earth masses.

When we glimpse briefly into this data, we can admire the real 'zoo' that exoplanets have become: orbiting stars of spectral types from F to M, minimum masses from $5 M_{\oplus}$ ⁴ to $20 M_J$ ⁵, periods from a little over of 1 day to 5218 days and eccentricities from perfect circular orbits to extreme values of more than 0.90. There are planets as close as 0.0177 AU and as far as 670 AU from their host stars.

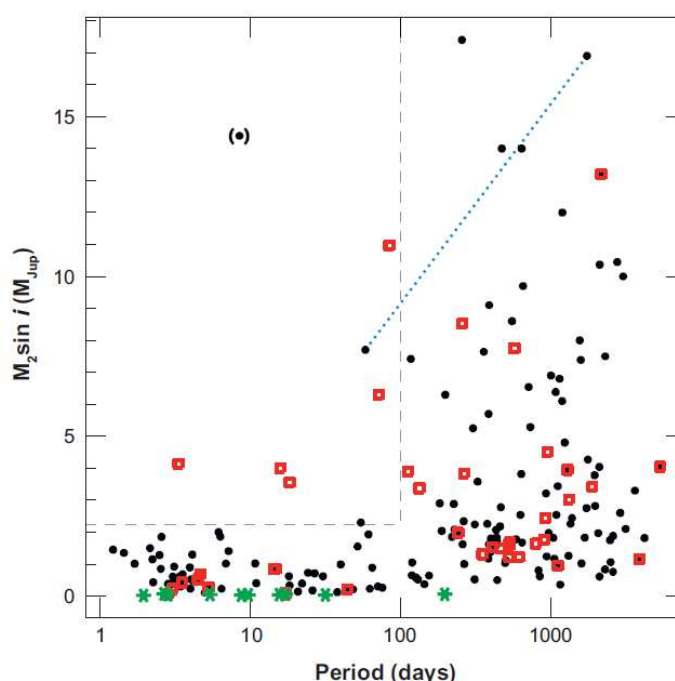


Figure 1.4: Plot of Period-Mass distribution of known exoplanets orbiting solar type stars. The black dots, red squares and green stars represent planets around single stars, planets in binaries and solid planets, respectively. The gray dashed lines represent a limit at $2.25 M_J$ and 100 days. The blue dotted line connects the two massive bodies orbiting HD 168433. The parentheses indicate the position of the probable brown dwarf HD 162020 (Udry & Santos 2007).

This information can be of great help in setting tighter constraints to planetary formation models. With this in mind, we can analyse the distributions of the eccentricities, periods and planetary masses and try to relate them among each other and

²<http://www.exoplanet.eu/catalog.php> (on 16/06/2008)

³excluding the pulsar systems with planets detected by pulsar timing

⁴Earth masses

⁵Jupiter masses

with other measured parameters like the host star properties (chemical composition, effective temperature, surface gravity, mass, age).

For instance, an illustration of the Period-Mass distribution of the known extrasolar planets orbiting solar type stars can be seen in Fig 1.4. We can clearly observe that there is a lack of massive planets in short period orbits. If we exclude multiple systems we can see that there is no planet with a mass greater than $2 M_J$ at all in orbits shorter than 100 days. This might be a consequence of a migration process or a mass transfer (or even absorption) of planets into the star (e.g. Trilling et al. 1998).

1.7 The Formation of Planetary Systems

Despite all this bounty of data, we still have a cloudy view of the physical mechanisms behind the formation of planetary systems. The appearance of giant planets close to the star and the existence of bodies with high eccentricity completely changed the way simulations were made. Quite simply, these cases never appeared in the computational models because the constraints used in the possible scenarios were based only on our Solar System...

Nowadays, there are two major theories about the formation of giant planets: core accretion and direct gravitational instability.

The first one tells us that planets are formed via accretion of dust grains. They continuously grow and collide with each other until they form planetesimals, with a few kilometers in diameter. These bodies continue to grow and collide until they reach bigger sizes, over the course of a few million years. If the mass of a protoplanet reaches 10 to 15 M_{\oplus} before the dispersion of the disk of gas, a runaway accretion will follow and a gas giant will form. On the contrary, if the mass doesn't reach the critical value necessary for runaway accretion, a smaller rocky planet or Neptune type planet will form (Pollack et al. 1996; Alibert et al. 2006).

The second one states that planets form by disk instability: the solar nebula breaks up, through its own self gravity, into clumps of gas and dust, rapidly forming proto-planetary bodies. They are expected to be massive gas giants, forming really fast with $\tau \sim 10^3$ years compared to the accretion time of $\tau \sim 10^6$ years in an optimistic scenario (Boss 1997).

The planets could then migrate or remain more or less in the location of formation. This will depend mainly on planet-disk interactions (Trilling et al. 1998).

The metallicity also seems to play an important role. This will be shown in more detail in subsection 1.8.1.

1.8 The Host Star Chemical Properties

In this section, we will discuss the chemical properties of the planet host stars. As we will see, these properties are providing important clues about the formation of planetary systems and its constraints.

1.8.1 The Metallicity Distribution

The analysis of the properties of stars with giant planets have revealed that a giant planet has a much higher probability to be found around stars that have, on average, a higher metallicity, at least for $[\text{Fe}/\text{H}]$ above the solar value (e.g. Gonzalez 1998; Gonzalez et al. 2001; Laws et al. 2003; Santos et al. 2001a, 2001b, 2003, 2004, 2005; Fischer & Valenti 2005). It was also shown that this result is not biased (e.g. Santos et al. 2003, 2004; Fischer & Valenti 2005). This means that metallicity has a crucial role in the formation and evolution of planets (at least for the giant ones). Interestingly enough, it seems that for low metallicities, the frequency of planets may remain constant (Santos et al. 2004). In Fig. 1.5, we can see two histograms of the frequency of planet hosts with $[\text{Fe}/\text{H}]$, where this behaviour is evident.

For Neptune class planets no such clear trend is observed. However, there aren't enough planets yet to make a sound statistical distribution (Udry et al. 2006, Sousa et al. 2008).

Shortly after this crucial observation, two different hypothesis for this 'anomalous' metallicity arose: the primordial origin and the external pollution process.

The first one defends that the high metal content of the star originated from the primordial cloud that gave origin to the planetary system. The detected metallicity is seen as nothing more than a consequence of the galactic chemical evolution. The host stars are simply in the high metallicity end of the distribution. This scenario was favoured in some recent studies (e.g. Sadakane et al. 2002; Santos et al. 2003, 2005; Fischer & Valenti 2005; Ecuivillon et al. 2006).

The second one posits that the high metallicity found in some stars is due to the late accretion of planetary material. Some evidence was found for this latter scenario: hints of pollution were discovered by Gonzalez (1998) in the 16 Cyg system in the form of an iron enhancement. This was later confirmed by Laws & Gonzalez (2001). However, Santos et al. (2001a) had noticed that the quantity of iron that is needed to explain the higher metallicity of a solar type star with this scenario is often much higher than expected, especially if we consider pollution as the dominant factor in the determination of the stellar metallicity.

These two mechanisms leave different imprints: in the former case, the star formed

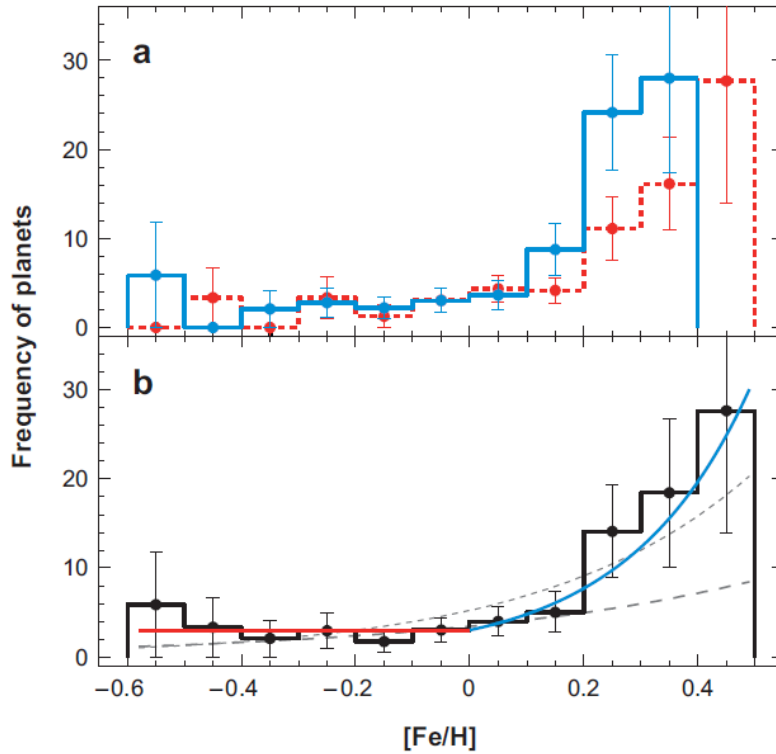


Figure 1.5: a) Percentage of planet hosts with stellar metallicity from CORALIE (blue) and Lick-Keck (red) samples. The lowest metallicity part of the histogram has few planet hosts and therefore its statistics are poor.; b) Average distribution of the two samples. The blue curve represents a power law fit of the data using only the $[Fe/H]$ values greater than 0.0. The red line represents an average value for $[Fe/H]$ between -0.5 and 0.0. (Udry & Santos 2007).

in a high metallicity cloud will be fully metal rich; in the latter case, the high metallicity is confined to the stellar convective zone but its interior is left metal poor. In this context, it is important to emphasise that F dwarfs with relatively thin convective zones should exhibit a greater degree of pollution (Fischer & Valenti 2005). Therefore, the upper part of the distribution of metal abundance of a F dwarf should exceed the highest value of G dwarfs. This was not observed. On the other hand, this pollution might dilute with the passage of time, mixing with deeper, unenriched layers (Vauclair 2004). Moreover, giant stars with planets, despite having larger convective envelopes, do not present a lower metallicity when compared to planet host stars similar to the Sun (Ecuvillon et al. 2006). A study on the abundances of elements other than iron might give us clues on this important question (see subsection 1.8.2).

It is true that pollution can be important in a few isolated cases. However, the most accepted view today is that pollution is only responsible for a small part in the global metallicity of the star.

This result has important implications for planetary formation theories. As we have seen in Section 1.7, there are two main models of planetary formation: core accre-

tion and gravitational instability. The former predicts that the efficiency of planetary formation depends on metallicity. The latter doesn't (Boss 2002). The fact that the probability of finding a giant planet increases with $[\text{Fe}/\text{H}]$ thus favours the core accretion model. This dependence can even be predicted by current models (Ida & Lin 2004a). However, it is not fully known how an increase in the metallicity will change the parameters that reign over the formation and evolution of planets.

1.8.2 Abundance of other Elements

For some time the spectroscopic studies were almost restricted to the measurement of the iron abundance ($[\text{Fe}/\text{H}]$) that acted as a metallicity proxy. Then, works on the abundance of other elements ($[\text{X}/\text{H}]$) gradually started to appear. Many studies were made to analyze, for example, the abundances of light elements (e.g. Sandquist et al. 2002; Israelian et al. 2003), alpha and iron peak elements (e.g. Gonzalez et al. 2001; Takeda et al. 2001; Bodaghee et al. 2003; Ecuivillon et al. 2004; Fischer & Valenti 2005; Beirão et al. 2005; Gilli et al. 2006).

Some interesting tendencies were found. The higher probability of finding giant planets around stars with higher metallicity was confirmed for many other elements other than iron (e.g. Bodaghee et al. 2003; Beirão et al. 2005; Gilli et al. 2006). In the study on the origin of the high metallicity of planet host stars, for example, Israelian et al. (2003) found out that HD82943 had a significant amount of ${}^6\text{Li}$ in its atmosphere. This is only possible if the star has engulfed lots of planetary material, because almost all original ${}^6\text{Li}$ is destroyed before the star enters in the main sequence and should not be detected (Sandquist et al. 2002). Therefore, this evidence favours the accretion of planetary materials scenario (see subsection 1.8.1). Hints of pollution were also found by Laws & Gonzalez (2001) in 16 Cyg in the form of a lithium enhancement.

On the other hand, Ecuivillon et al. (2006) showed that there is no increase of $[\text{X}/\text{H}]$ with the condensation temperature for volatile and refractory elements, contrary to what should be expected if pollution was the main cause of the metallicity excess (i.e. volatiles of the planet should evaporate before the accretion takes place).

Despite that, it's worth noting the strange behaviour of $[\text{X}/\text{Fe}]$ of some elements (e.g. Mg, Mn, V, Co) on planet host stars found by some authors (Bodaghee et al. 2003; Gilli et al. 2006). This is very difficult to explain by galactic chemical evolution models but these differences might be related to NLTE⁶ effects (Bodaghee et al. 2003). The enhanced abundances of Si and Ni might also increase the giant planet formation efficiency (Robinson et al. 2006).

⁶Non-Local Thermodynamic Equilibrium

1.8.3 Correlations between Metallicity and Orbital Parameters

The possible correlations between metallicity and orbital parameters have been studied (e.g. Gonzalez 1998; Santos et al. 2003; Fischer & Valenti 2005). No clear correlation has surfaced. However, stars with short period planets seem to be particularly metal rich. Ida & Lin (2004b), in their work on the planetary formation modelling, have shown that a higher metallicity might allow a formation of giant planets faster or/and closer to their host star. Therefore, the planets should have more time to migrate, and this could explain the yet fragile correlation. On the other hand, if the migration is fast enough, this correlation might have little meaning.

1.9 Our Work

Following the previous works on the abundances of iron and other elements we will derive the abundances of twelve species (silica, calcium, titanium, scandium, manganese, chromium, vanadium, cobalt, nickel, sodium, magnesium and aluminium), based on the spectra of a subsample of one of the HARPS⁷ 'high precision' GTO⁸ planet search program containing 451 stars. Of these, 66 are planet hosts and the other 385 stars are dwarfs with no known orbiting planet.

In order to achieve this goal we will use VALD⁹ to obtain the initial list of the spectral lines; use IRAF¹⁰ to identify and select the good spectral lines; use ARES¹¹ to automatically measure the equivalent widths (EWs) of the lines of interest; use MOOG (Sneden 1973) to calculate the abundances of the species of interest and create a FORTRAN program to use the necessary programs and to organise the final abundances in an easy-to-use database.

The preparatory steps that precede the derivation of the final abundance values as well as the discussion on the uncertainties of the analysis will be explained in chapter 3. Then, the discussion of the results will follow in chapter 4: we will see if there are any differences in the distributions and trends of the stars with and without planets. Lastly, in chapter 5, we will make some concluding remarks and draft the possible future investigations. In the next chapter we will give a brief outlook on the determination of chemical abundances: the local thermodynamic equilibrium, the EW calculation and its dependence on the different physical parameters and the calculation of the abundance with differential analysis.

⁷High Accuracy Radial Velocity Planetary Searcher

⁸Guaranteed Time Observations

⁹Vienna Atomic Line Database

¹⁰Image Reduction and Analysis Facility

¹¹Automatic Routine for line Equivalent widths in stellar Spectra

Chapter 2

Determination of the Chemical Abundances

This chapter is based in Gray (2005). We will present a brief outlook on the determination of chemical abundances in a solar type star. For a more profound insight refer to chapter 13 (The Behaviour of Spectral Lines) and 16 (Chemical Analysis) of Gray (2005). All pictures are taken from this book except when said otherwise.

2.1 Introduction

If we take a good look at a regular stellar spectra we can easily identify the presence of many absorption lines. These lines correspond to electronic transitions among the different levels of the atoms in the stellar atmosphere (bound-bound transitions). This is especially true for cooler stars of the FGKM end of the HR diagram, where the atoms and molecules of many species are not fully ionised. The elements other than hydrogen and helium, referred as 'metals', only account for a tiny percentage of the abundance. However, most spectral lines have origin in these metal species.

These lines show different shapes and strengths that derive directly from the conditions in the photosphere of the star (temperature, pressure, radiation, magnetic and velocity fields). The most important aspect in the determination of an element's abundance is that the strength of the line absorption depends on the number of absorbers that correspond to that transition.

2.2 Local Thermodynamic Equilibrium

If we consider that collisions (rather than radiation) dominate the excitation of the atoms (as a good approximation in the case of solar type stars), then local thermody-

dynamic equilibrium (LTE) will apply and we can express the ratio between the number of atoms in a level n and the total number of the atoms of that species as

$$\frac{N_n}{N} = \frac{g_n}{u(T)} 10^{-\theta(T)\chi_n}, \quad (2.1)$$

where N_n is the population of level n , N is the total number of atoms, g_n is the degeneracy of level n , χ_n is the excitation energy of the same level, $\theta(T) = 5040/T$, $u(T) = \sum g_i e^{-\chi_i/kT}$ is the partition function, k is the Boltzmann's constant and T is the temperature. This is one formulation of the well known Boltzmann equation.

Similarly, the ionisation for the collision dominated gas can be calculated using Saha's Equation,

$$\frac{N_1}{N_0} = \frac{\Phi(T)}{P_e}, \quad (2.2)$$

where

$$\Phi(T) = \frac{(\pi m_e)^{3/2} (2kT)^{5/2}}{h^3} \frac{u_1(T)}{u_0(T)} e^{-I/kT}. \quad (2.3)$$

The N_1/N_0 is the ratio of ions in a given ionisation state to the number of neutral atoms, u_1/u_0 is the ratio of ionic to neutral partition functions, m_e is the electron mass, h is the Plank's constant, P_e is the electron pressure and I is the ionisation potential.

Thermodynamic equilibrium is achieved when the temperature, pressure and chemical potential of a system are constant. In LTE, these thermodynamic parameters are varying in space and time but this variation is slow enough for us to assume that, in some neighbourhood about each point, thermodynamic equilibrium exists (hence the 'local'). When the LTE is valid, each point will behave like a black body of temperature T . This is, of course, an approximation, but it is acceptable for the cases when the ratio of collision to radiation induced transitions is large, as it is the case for photospheres of stars similar to the Sun. In the outer photospheric layers, LTE performs poorly due to the proximity of the open space boundary, where the radiation can escape freely. This boundary is responsible for the formation of the absorption lines. We cannot use strong lines calculated by LTE because their cores form in these upper layers.

As we will see in the following sections, LTE will be used to calculate our model atmosphere and help us find the abundances of the species of interest. We must recall that the temperature in the LTE approximation is the same for all physical processes: thermal velocity distributions, ionisation equilibrium, excitation of atomic populations. It's a huge simplification over the real problem but it is very practical.

2.3 The Behaviour of Line Strength

The strength or equivalent width (EW) of a spectral line depends on the absorption coefficient (the fraction of incident radiant energy absorbed per unit mass or thickness of an absorber) and on the number of absorbers, derived from Eqs. (2.1) and (2.2). This implies that the line strength depends on temperature, electron pressure and the atomic constants. This is valid only as a good approximation for weak lines (i.e. lines with typical $EW \lesssim 200 \text{ m}\text{\AA}$). Stronger lines may depend on other factors.

In the next subsections we will see how to measure the EW and, from there, how the abundance, temperature and pressure can influence the line strength of absorption lines. We will restrict our analysis to weak lines, because they are the ones that will be measured for a posterior determination of the abundance.

2.3.1 The Measurement of the EW

Equivalent width is a measure of the intensity of a spectral line. It is defined as the width of a rectangle with height between the level of the continuum, normalised to unity, and the reference zero, having a surface equal to the profile of the spectral line, as shown on Fig. 2.1.

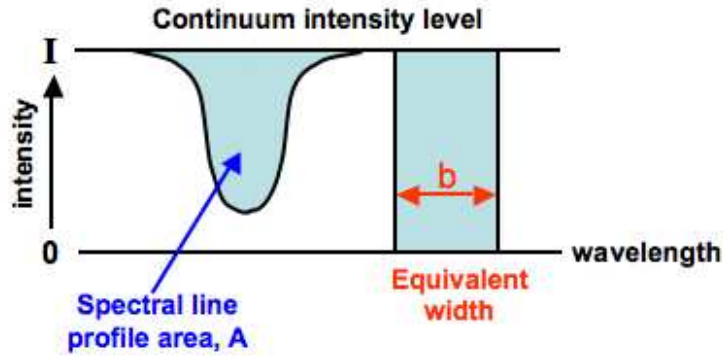


Figure 2.1: Illustration of a spectral line and its equivalent width. From: <http://astronomy.swin.edu.au>.

The EW is thus measured in wavelength units (\AA or $\text{m}\text{\AA}$). Mathematically we have

$$W = \int_{-\infty}^{\infty} \frac{I_c - I_\lambda}{I_c} d\lambda, \quad (2.4)$$

where I_c is the intensity of the continuum and I_λ is the intensity of the wavelength at each $d\lambda$. Usually, the EWs are measured by fitting a gaussian function to the spectral line and to the local continuum. We must note that, in some of the following plots, the equivalent width will be represented by W .

From the accurate measurement of the EW of weak lines we can get the abundances of species and also calculate some stellar parameters (e.g. temperature, surface gravity, microturbulence).

2.3.2 The Abundance Dependence

The abundance is one of the most important factors in the line strength variation. As the abundance increases, line strength also increases, as expected. However, the EW does not change linearly with abundance, as we can see in Fig. 2.2a.

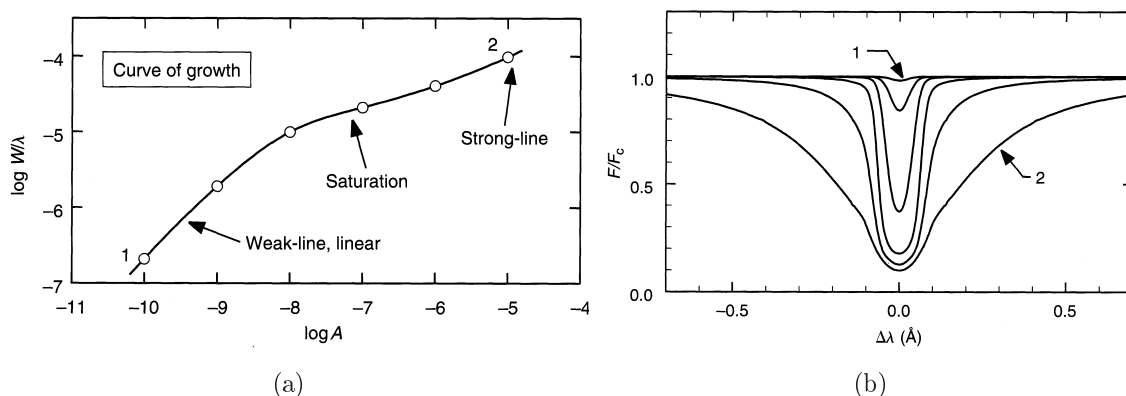


Figure 2.2: a) Typical curve of growth from a model photosphere: log-log plot of the reduced EW (W/λ) with abundance (A).; b) Line profile change with chemical abundance of the absorption species. The dots in (a) correspond to the different lines in (b).

There are three different regimes. The first one corresponds to the weaker line behaviour, where the core dominates and the EW is proportional to the abundance A . The second phase begins when the central depth approaches the maximum value and the line saturates and grows asymptotically towards a constant value. The third one starts as the optical depth of the line wings becomes significant compared to the absorption of the continuum. We are only interested in the first phase, where the behaviour of the curve is linear.

Every spectral line shows a similar behaviour. A plot like Fig. 2.2a is called a curve of growth. Fig. 2.2b shows the line profile change with the chemical abundance of the absorbing species.

2.3.3 The Temperature Dependence

Temperature is the most important variable in determining the line strength. This can be easily seen in the excitation and ionisation process equations (section 2.2). We can appreciate the behaviour of the EW of a typical weak line with T_{eff} depicted by Fig. (2.3). Four different cases are shown:

1. weak line of a neutral species with the element mostly neutral.
2. weak line of a neutral species with the element mostly ionised.
3. weak line of an ion with the element mostly neutral.
4. weak line of an ion with the element mostly ionised.

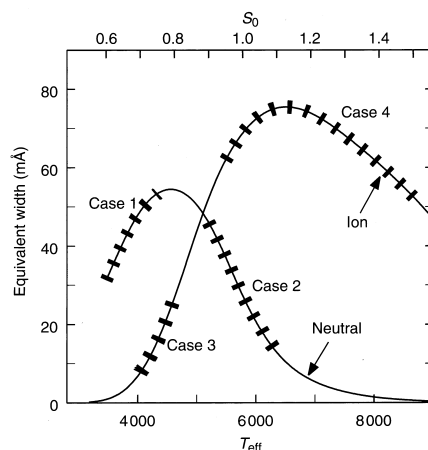


Figure 2.3: Plot of the behaviour of the EW of typical weak metal lines with T_{eff} . The cases discussed in the text are shown.

In cases 1 and 3 an increase in T_{eff} leads to an increase in the line strength. This also happens in case 4 up to a maximum value of EW. The decrease in strength can be accounted for due to the increase in the continuum absorption from the negative hydrogen ion (case 4) or due to the ionisation of the absorbing species (case 2). In any case, we can predict how a certain line will grow or weaken by considering the ratio of the line absorption coefficient with the continuum absorption coefficient. If the former coefficient increases/decreases, the line will grow/weaken. However, if the latter increases/decreases, the line will get weaker/stronger.

Note that the weakening of the line due to an increase of the continuum absorption also affects the lines in case 1 and 3. However, this effect is weak compared to the excitation one.

The direction and strength of change will depend on the T_{eff} and on the excitation potential (the minimum energy that an electron of a certain atom needs to make a successful transition between the ground state and an excited state) of the line. For stars similar to the Sun, cases 2 and 4 apply because most elements are ionised. Solar lines of neutral species almost always decrease in strength with T_{eff} , but ionised species have the opposite behaviour.

2.3.4 The Pressure Dependence

The pressure effects are visible in different ways. The dominant effect in weak lines is the change in the ratio of line absorbers to the continuum absorption (due to the H^- ion in solar type stars). To account for pressure effects we must consider gas pressure (P_g) and electron pressure (P_e). In cool stars, the pressure can be approximated by $P_g \approx Cg^{2/3}$ and $P_e \approx C'g^{1/3}$, where C and C' are constants and g is the stellar surface gravity. In this case, pressure changes can be translated into approximate gravity dependences for the F, G and K stars, which is our case. We can see such dependence illustrated in Fig. 2.4.

It's important to emphasise that pressure effects in stellar spectra are much weaker than temperature effects. For weak metal lines in cool stars, we can enumerate the following rules, based on Eq. 2.2:

1. weak lines formed where most of the element is in the next higher ionisation stage are insensitive to pressure changes.
2. weak lines formed where most of the element is in that same ionisation stage are pressure sensitive: lower pressure cause greater line strength.
3. weak lines formed where most of the element is in the next lower ionisation stage are very pressure sensitive. Lower pressure enhances the lines.

Regarding solar type stars, where most metals are ionized, cases 1 and 2 are more common (neutral and first ion species, respectively).

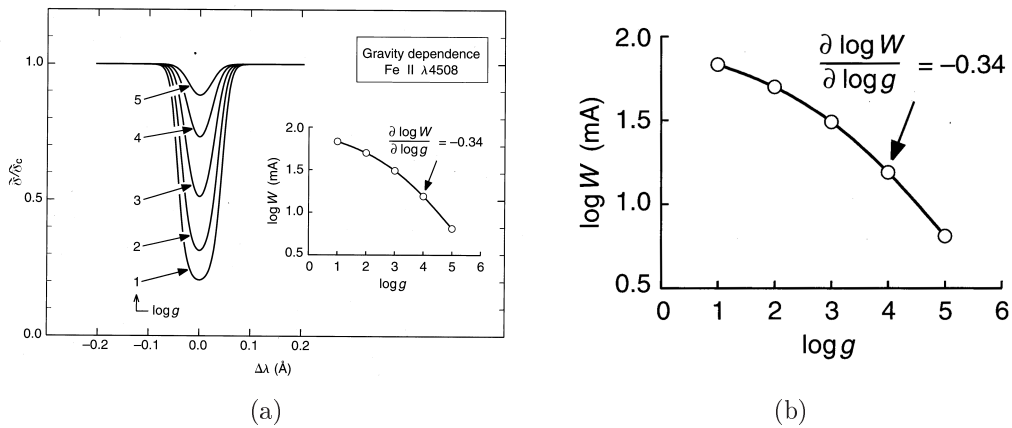


Figure 2.4: a) Profiles of FeII $\lambda 4508$ shown for several values of surface gravity (in cm/s^2). The inset is shown in (b) for clarity; b) log-log plot of EW with surface gravity. The values of $\log g$ in (a) correspond to the dots in (b).

If the surface gravity ($\log g$) is unknown, it can be determined by forcing the ion and neutral solutions to give the same abundance (spectroscopic surface gravity), since the former are pressure dependent and the latter are insensitive to pressure changes.

2.3.5 Microturbulence and Velocity Fields

In the analysis of line profiles we should be aware that photospheric velocity fields (the turbulence) introduce Doppler shifts, that will be reflected in the spectra: the small scale motion, microturbulence, can affect the radiation transfer and the large scale motions, macroturbulence and rotation, introduce a broad distribution of Doppler shifts that reshapes the line profile, but does not change its EW.

Microturbulence is almost always incorporated into abundance analysis because it explains that the EW of saturated lines are smaller or greater than predicted. The Fig. 2.5 shows the effect of microturbulence on the curve of growth. As we can see, changes in microturbulence can change the shape of the curve of growth and consequently the measured abundance.

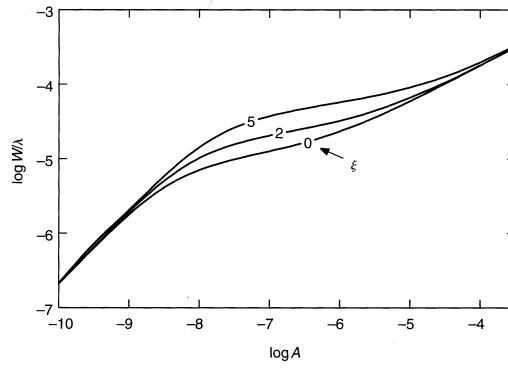


Figure 2.5: Curves of growth with different values of microturbulence

2.4 Calculation of the Abundance

The abundance of an element will be derived from the the EWs of the corresponding spectral lines. Assuming that all stellar and atomic parameters are correct and that we have a correct LTE based atmosphere calculated, we know the populations of the atoms and ions in their different levels. Then, using a radiative transfer program with differential analysis (see subsection 2.4.1) such as MOOG (Snedden 1973) we can use the Sun and the star EWs and the atomic/stellar parameters to calculate the relative abundances of a star. This will be explained in detail in chapter 3.

If the parameters are correct, we should obtain an abundance that is independent of the excitation potential and of the EW. Moreover, the abundance of the neutral atom of a species should be equal to the abundance of the ion of the same species. If they are not, there must be an error in some value of the stellar parameters, in the measured EWs or even in the model itself, in the case that NLTE effects became

important. Errors can grow a lot if we have few lines to measure the EW, where line blending is severe (mostly in cooler stars) or where atomic constants (or/and stellar parameters) are not well known.

2.4.1 Differential Analysis

Differential analysis consists in comparing abundances between stars. It can only be applied to stars with similar stellar parameters, especially effective temperature and surface gravity. This is our case. The comparison is made between a reference star (usually the Sun) and a star of unknown composition, deriving the value A/A_{ref} for the elements of interest, where A_{ref} is the abundance of the reference star. The atomic parameters for each line are the same for both stars. Only the EW changes. The output abundance will be the logarithm of the abundance of the star to the solar abundance and will be denoted as $[X/H] = \log[A(X)_{star}/A(X)_{\odot}]$ and $A(X) = N_X/N_H$, where N_X is the number of atoms of the X element and N_H is the number of atoms of hydrogen.

One of the advantages of differential analysis is that one can derive the astrophysical oscillator strength values, instead of using laboratory measurements that may not have sufficient precision. These values are obtained via an inverse analysis: we start with the known abundances and the EW of a certain species line for the Sun and we determine its oscillator strength (expressed as $\log gf$, where g is the degeneracy and f is the strength of the electronic transition). The same oscillator strength value will be used in both stars, thus minimizing the internal errors. This is detailed in subchapter 3.3.4. However, this has an intrinsic disadvantage: strictly speaking, the calculated $\log gf$ are only 100% reliable for the Sun and the analysis gets worse as we get further away from the Sun's parameters.

We need to note that deviations from LTE typically cause errors of no more than a few percent, in Solar type stars. We also need to note that this abundance is only valid in the atmosphere of the star.

The solar composition is a standard for many differential stellar analysis and for the basic chemical mix entering many stellar photosphere models. The mass fraction used is typically $X=0.735$ for hydrogen, $Y=0.248$ for helium and $Z=0.017$ for all other elements. One can obtain the reference abundance values of the Sun from, for example, Anders & Grevesse (1989).

Chapter 3

Data and Spectral Analysis

The details of the technique used for the determination of the abundances will be explained in the following chapter. It's important to emphasise that this is an homogeneous study. It means that the spectra used to measure the EW of the atomic lines were taken with the same instrument (HARPS), reduced/normalised with the same methodology and that the calculated atomic and stellar parameters were based on the same atmospheric models and line lists.

3.1 The HARPS Spectrograph

HARPS is a fibre-fed, cross dispersed echelle spectrograph. It operates at a constant temperature of 17°C, and at a constant pressure $< 10^{-2}$ mbar. It is located in the Coudé floor of the ESO¹ La Silla 3.6 m telescope. Two fibres, an object and a reference fibre, fed the spectrograph with light from the telescope and from the calibration lamps (or sky). The light is reimaged by the internal optics onto a mosaic of two 2k4 CCDs² where two spectra of 72 orders are formed. The spectral range goes from 380 to 690 nm. At a resolution ($R \equiv \lambda/\Delta\lambda$) of 115.000, each spectral element is sampled by 3.2 CCD pixels. For further details refer to Mayor et al. (2003).

3.2 Spectral Data

The spectra for the HARPS 'high precision' GTO program was obtained with the HARPS spectrograph at the ESO La Silla 3.6 m telescope. This sample is composed of 451 stars selected from the volume limited sample of solar neighbourhood stars studied with the CORALIE spectrograph (Udry et al. 2000) as well as a group of planet host

¹European Southern Observatory

²Charge-Coupled Devices

stars from the southern hemisphere. The total number of planet-bearing stars is 66. Every star in the catalogue is slowly rotating, non evolved and with a low chromospheric activity. For a more detailed description see Sousa et al. (2008).

The main goal of the GTO program is the detection of very low mass exoplanets aiming to push the RV accuracy below $1m/s$ (Mayor et al. 2003). We will use the high resolution high S/N³ spectral samples of this program to calculate the abundances.

The individual spectra were reduced using the HARPS pipeline and later combined using IRAF after correcting for its radial velocity. The final spectra have a resolution of $R \sim 115.000$ and a signal to noise ratio ranging from ~ 70 to ~ 2000 depending on the amount and quality of the original spectra. Nine tenths of the spectra have S/N higher than 200.

A solar spectrum was also collected with HARPS using solar light reflected by the asteroid Ceres. This spectrum has the same resolution of the star's spectra and a S/N ratio of ~ 250 .

A sample of the 'high precision' GTO catalogue is shown in Table 3.1. The stellar parameters of this table were determined by Sousa et al. (2008). The full catalogue is available at http://www.astro.up.pt/~sousasag/harps_gto_catalogue.html.

Table 3.1: Sample table of the HARPS GTO 'high precision' spectroscopic catalogue. Each line gives the star's name, effective temperature (T_{eff}), spectroscopic surface gravity ($\log g_{spec}$), microturbulence (ξ_t), metallicity ([Fe/H]), signal to noise ratio of the spectrum (S/N) and if the star hosts planets. All parameters were obtained by Sousa et al. (2008).

Star ID	T_{eff} [K]	$\log g_{spec}$ [$cm\ s^{-2}$]	ξ_t [$km\ s^{-1}$]	[Fe/H]	S/N	planet host?
...
HD117207	5667 ± 21	4.32 ± 0.04	1.01 ± 0.02	0.22 ± 0.02	252.60	yes
HD117618	5990 ± 13	4.41 ± 0.02	1.13 ± 0.01	0.03 ± 0.01	613.22	yes
HD119638	6069 ± 16	4.42 ± 0.03	1.22 ± 0.02	-0.15 ± 0.01	1163.50	no
HD119782	5160 ± 34	4.44 ± 0.06	0.79 ± 0.07	-0.07 ± 0.02	479.70	no
HD121504	6022 ± 11	4.49 ± 0.03	1.12 ± 0.01	0.14 ± 0.01	526.01	yes
HD122862	5982 ± 13	4.23 ± 0.02	1.29 ± 0.01	-0.12 ± 0.01	1338.76	no
HD123265	5338 ± 44	4.29 ± 0.07	0.85 ± 0.08	0.19 ± 0.03	354.26	no
HD124106	5106 ± 39	4.49 ± 0.08	0.80 ± 0.09	-0.17 ± 0.03	361.54	no
HD124292	5443 ± 22	4.37 ± 0.04	0.77 ± 0.03	-0.13 ± 0.02	975.63	no
HD124364	5584 ± 14	4.48 ± 0.02	0.83 ± 0.02	-0.27 ± 0.01	451.62	no
...

³Signal to Noise ratio

3.3 Identification and Selection of the Spectral Lines

The first part of this work consisted in the identification and selection of the weak spectral lines of the following species: alpha group elements (Si, Ca, Ti, Sc), iron peak elements (Mn, V, Cr, Co, Ni) and also Na, Mg and Al. The absorption lines of some of the first ionised species (TiII, ScII, CrII) were also selected. The species with absorption lines from both the neutral atom and the ion will be denoted as XI (for the neutral atom) and XII (for the ion) throughout this work, where X=Ti, Sc or Cr.

Fig. 3.1 illustrates the most important steps in the process of identification and selection of the spectral lines. These steps will be described in detail in the following subsections.

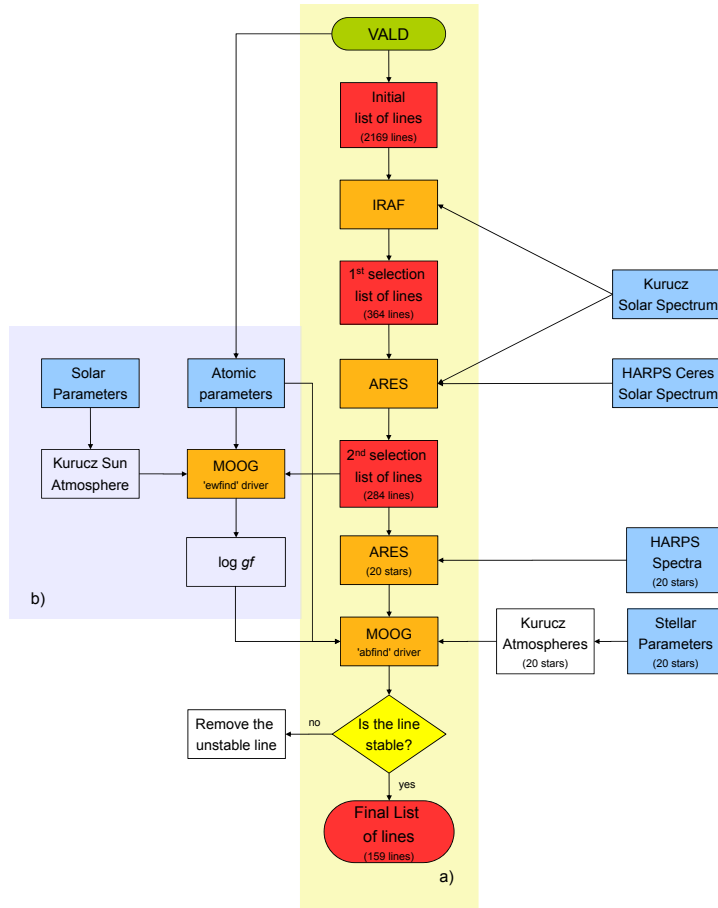


Figure 3.1: Diagram illustrating the most important steps necessary in the identification and selection of the spectral lines. The green and red rounded rectangles represent the beginning and the end of the process. The blue rectangles represent input parameters (spectra, stellar and atomic parameters). The orange rectangles symbolize the different programs (IRAF, ARES, MOOG) used throughout the process. The white rectangles designate intermediate steps. The red rectangles represent the selection progress of the list of lines and the yellow diamond a decision on the stability of the selected lines. a) illustrates the process of line identification and selection, from the acquisition of the lines at the VALD database to the final list of lines; b) shows the necessary steps needed to calculate the astrophysical oscillator strengths.

3.3.1 Using VALD to Obtain the Initial List of Spectral Lines

Our study started with a request at the Vienna Atomic Line Database (VALD - Kupka et al. 1999) of every spectral line (including the lines of the species that will be investigated) and its atomic parameters (wavelength, oscillator strength, excitation potential) from 4500 to 6910 Å. The request was done via the internet⁴.

Inside VALD, the 'extract stellar' option was chosen and the following parameters were inserted: Spectral Region: 4500 – 6910 Å; $T_{eff} = 5777$ K; $\log g = 4.44$ dex⁵; $\xi_t = 1.0$ km/s; detection limit = 0.05, where T_{eff} is the effective temperature, $\log g$ is the surface gravity and ξ_t is the microturbulence of the star. The stellar and atomic parameters inserted in the model are those of the Sun. The 'detection limit' option was set to 0.05, meaning that only the spectral lines with central depths greater than 5% of the continuum were accepted. The goal here was to use the most approximate model of the Sun as possible in order to obtain the relevant spectral lines in a solar type star.

The acquired output contained the wavelength, excitation potential, estimated line depth and oscillator strength for each spectral line. The 'extract stellar' option has the advantage of supplying all the spectral lines. This will help to identify lines that overlap with the lines of interest in the subsequent analysis of the spectra.

3.3.2 Using IRAF to Identify the 'Good' Lines

With IRAF⁶ plot tool, we opened a noiseless synthetic spectrum of the Sun (Kurucz Solar Flux Atlas - Kurucz et al. (1984)) with an extremely high resolution and we carefully checked for the existence of the lines of interest.

We only chose isolated or lightly blended lines. Then, we measured their EW. All lines with EWs lower than 5 mÅ or inside the wings of strong lines (e.g. H_α ($\lambda = 6562.81$ Å), H_β ($\lambda = 4861.34$ Å) and strong $\lambda 5172.70$, $\lambda 5183.62$ Mg I lines) were excluded. A classification system was made, ranging from 1 (blended, distorted or hard to read lines) to 5 (totally isolated lines). 364 lines were selected in this first phase, from an initial list of 2169 lines.

It's worth noting two things regarding the manual measurement of the EW of the spectral lines using IRAF: 1) we should always choose a region of at least 1 Å to each side from the centre of the line of interest and deconvolute all lines in that region; 2) when measuring a line we should never target the pointer to any place above the continuum: this can lead to an overestimation of the EW.

⁴<http://www.astro.uu.se/~vald/>

⁵decimal exponent

⁶<http://iraf.noao.edu/>

3.3.3 Measuring the EWs of the Solar Lines with ARES

We used ARES (Automatic Routine for Line Equivalent Widths - Sousa et al. 2007) to automatically measure the equivalent widths of our lines. First, we analysed the lines of two different spectra: one is a resolution degraded spectrum made from the Kurucz Solar Flux Atlas ($R = 110.000$) and the other is a spectrum of the Sun's reflected light from the Ceres asteroid taken with the HARPS spectrograph⁷, with $R \sim 115.000$ and $S/N \sim 250$.

The measurement of the EWs was done one line at a time and was monitored with a graphical interface (plots_flag=1 within the 'mine.opt' file). This way we could see if the lines were being fitted properly.

The EW measurement in these very similar spectra allowed us to establish a tighter criteria: 1) if we obtained $|(EW_{Kurucz} - EW_{Ceres})/EW_{Kurucz}| > 0.10$ for the same line we discarded this line; 2) then, every line with $|EW_{Kurucz} - EW_{Ceres}| > 1 \text{ m\AA}$ was investigated to see if it was subjected to blending effects and discarded if appropriate. These criteria are important because the abundance is very sensitive to variations in the EW.

In order to optimise the calculation of the EWs, we chose the following ARES parameters (within the 'mine.opt' file): smoother = 4, space = 2, lineresol = 0.07, miniline = 5 and rejt = 0.996, where 'smoother' is a parameter to adjust the noise smoothing (1 to 4, the bigger the number, the greater the smoothing produced in the first derivative of the spectrum), 'space' is the interval, in Angstrom, used for the computation of each line; 'lineresol' sets the line resolution (in \AA) of the input spectra (if the program finds two lines closer than this value he will treat them as one line), 'miniline' is the minimum value of line strength (in m\AA) accepted to write a line in the output file and 'rejt' is a parameter for the calibration of the normalised continuum (0 to 1). The 'rejt' is the most important parameter for the correct automatic determination of the continuum (Sousa et al. 2007, Sousa et al. 2008). The higher the S/N ratio the higher should be the rejt parameter value.

We also repeated the classification process for both spectra. All lines with classification 1 were rejected and lines with classification 2 were investigated and discarded when appropriate. Additionally, all lines situated in regions of strong variation of the continuum as well as lines with bad fits were excluded. At the end of the process, we had a new list with 284 lines.

⁷Collection of HARPS solar spectra: <http://www.ls.eso.org/lasilla/sciops/3p6/harps/monitoring/sun.html>

3.3.4 Calculating New Oscillator Strengths

The EWs of the new list of lines and a Kurucz grid model for the Sun (Kurucz 1993) (having $T_{eff} = 5777$, $\log g = 4.44$, $\log \epsilon_{Fe} = 7.47$ and $\xi_t = 1.0$, where $\log \epsilon_{Fe}$ is the solar abundance of iron relative to hydrogen as used by Santos et al. 2004) were used to calculate new semi-empirical atomic oscillator strengths for the spectral lines from an inverted solar analysis. This is necessary because the $\log gf$ values obtained from VALD may not be accurate enough. The new oscillator strengths will be used to make a better differential analysis. This implies, of course, that the derived abundance values will always be relative to the Sun.

The calculations of the $\log gf$ were carried out with the 'ewfind' driver of the 2002 version of the LTE stellar line analysis program MOOG (Sneden 1973). The fixed solar abundances used in MOOG were taken from Anders and Grevesse (1989). The excitation potential and the initial value of $\log gf$ of every line came from the VALD database, as referred in subsection 3.3.1. All input parameters for 'ewfind' were taken following Santos et al. (2004).

The calculation of the new $\log gf$ values was done with an iterative FORTRAN program. For each individual line, we input at MOOG the fixed excitation potential, the fixed solar EWs and a variable value of the oscillator strength (starting with the $\log gf$ provided by VALD). At the end of each iteration, we got a certain value of the abundance as output. The true value of $\log gf$ is obtained when the value of the abundance for each element equals its solar abundance. In order to achieve the convergence of abundances, we used a simple bisection method in the iteration. It takes no more than a few minutes to obtain the correct $\log gf$ for all lines.

If we invert this analysis, we can use the new oscillator strengths to obtain the abundance of any element for every star.

3.3.5 A Test using the Solar Abundance Values

In order to confirm that the calculated $\log gf$ values were correct, we made a test using the measured EWs of the Sun's Ceres spectrum and a Kurucz (1993) atmospheres model (with the solar parameters) to calculate the abundances using MOOG 'abfind' driver. This time, we did the inverse analysis: the $\log gf$ and the EW values were fixed and the abundance was made to converge to a value corresponding to the fixed $\log gf$ and EW values. The average values of the abundances are within 0.01 dex of the expected value except for Al ($\Delta A = 0.03$ with 2 lines), ScI ($\Delta A = 0.03$ with 3 lines) and V ($\Delta A = 0.02$ with 14 lines), where A is the abundance of a species. However, the derived abundance of these three species are well within the abundance errors determined by Anders &

Grevesse (1989). Despite that, we shall check them for biases. No further lines were removed from the line list at this point.

3.3.6 The Molecular Equilibrium

Some of the analysed species may form molecules. This tendency increases for lower temperatures and can change the abundance of the element in question, if not properly corrected. Obviously, this effect is stronger in cooler stars.

In order to find if the use of molecular equilibrium was needed to correct the abundance of certain species, we measured the EWs using ARES and calculated the abundances for the coolest star in our sample, HD218511, using the MOOG code ('abfind' driver) and a Kurucz model atmosphere with the star's parameters ($T_{eff} = 4556$, $\log g = 4.31$, $\xi_t = 0.41$, $[Fe/H] = -0.10$). This calculation was done with two different values of the 'abfind' driver parameter 'molecules'. If 'molecules' was set to zero, MOOG would not use molecular equilibrium. If molecules was set to one, MOOG would calculate the abundance with the molecular equilibrium correction. No change in the abundance of any element was found. Therefore, we chose not to use molecular equilibrium when calculating the abundances.

3.3.7 Testing a small sub-sample Containing 20 Stars

In order to finish the selection of the spectral lines, two different groups of stars were chosen. The first group contained 10 stars with T_{eff} closer to 5000 K, hereafter 'cool group'. The second group contained 10 stars with T_{eff} closer to the Solar temperature (5777 K), hereafter 'hot group'. We will calculate the abundance of both groups separately and then we will observe the dispersion and difference to the mean value of abundance of each line, for every element and star, and make the selection of the lines based on appropriate criteria.

This analysis is very important. With it, we can find lines that yield systematically wrong abundance values due to an incorrect measurement of the EW (originated in blending effects - stronger in cooler stars - or in a poor position in the continuum), due to errors of the analysis methodology (the differential analysis used is based on the Sun and the further away a star is from the Sun's parameters the greater the errors the analysis will yield: this is especially true for temperature differences), or simply due to systematic errors of unknown origin.

First, we measured the EWs with ARES. The input parameters were the same as the ones used in subsection 3.3.3 except 'rejt' that changed with the S/N ratio of each star, according to Sousa et al. (2008).

Then, we made a small FORTRAN program that used the 'abfind' driver within MOOG and a grid of Kurucz (1993) ATLAS9 atmospheres to calculate the abundance of the individual elements. We can see in Fig. 3.2 the difference between the abundance of each line and the mean abundance of the respective star, for Ni, shown as example. The red and the blue dots correspond to the 'hot' and 'cool' groups respectively. The mean value of this difference will be referred as ΔA . The cyan and black crosses are the ΔA of the hot and the cool group, respectively, and the error bars represent the standard deviation (σ) of these mean values.

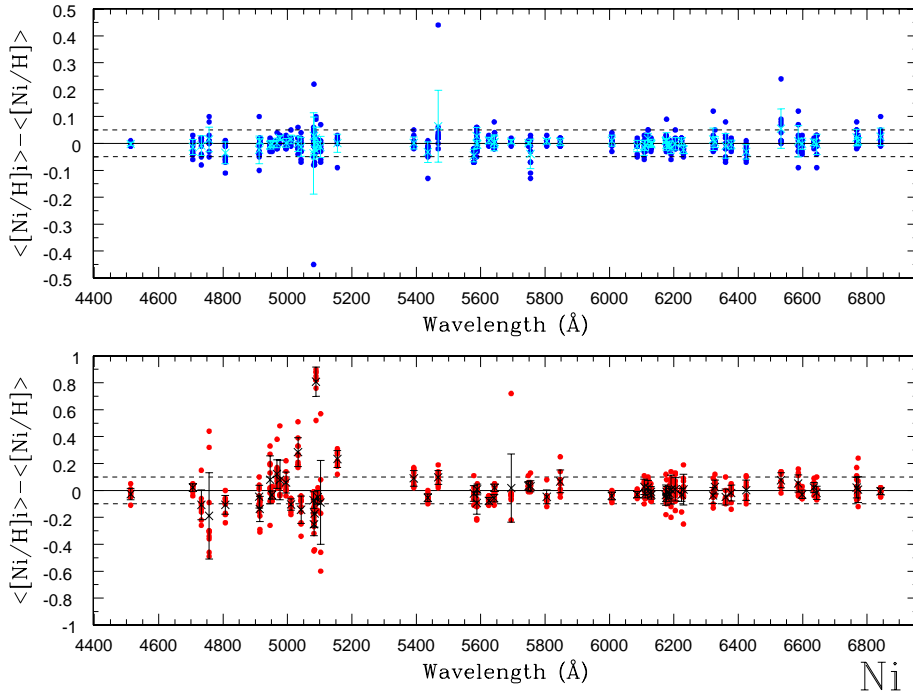


Figure 3.2: Selection of the stable lines for Ni based on an analysis of 20 stars. The red and the blue dots correspond to stars with $T_{eff} \sim T_{\odot}$ and $T_{eff} \sim 5000$ K, respectively. The cyan and black crosses are the mean value of the difference between the abundance of each line and the mean abundance of the respective star. The error bars represent the standard deviation of the mean values.

Following the analysis of Fig. 3.2, the lines were selected according to two different criteria: 1) all lines within the hot group with ΔA or/and with a dispersion greater than 0.05 dex were excluded; 2) all lines of the cool group with ΔA or/and with a dispersion greater than 0.1 dex were excluded. It was taken great care in identifying stray points clearly out of the 2σ distribution (due to bad pixels, cosmic rays or other unknown effects) that could alter the true value of the mean or the dispersion of a certain line. This is the case, for example, of the 5468.11 Å line in the hot group or the 5694.99 Å line in the cold group that could have been excluded if the criteria was strictly obeyed.

3.4. SPECTRAL ANALYSIS OF THE FULL SAMPLE

After the selection of the spectral lines according to this criteria, we created a final list with 159 lines, as shown in Table 3.2.

Table 3.2: Atomic parameters and measured solar equivalent widths of the spectral lines used to determine the abundance of the elements. Each lines give the wavelength (λ), the excitation potential (χ_I), the oscillator strength ($\log gf$) and the Solar EW. The lines of the neutral species are denoted as X I and the lines of the ions are denoted as X II.

λ (Å)	χ_I (eV)	$\log gf$	EW $_{\odot}$ (mÅ)	λ (Å)	χ_I (eV)	$\log gf$	EW $_{\odot}$ (mÅ)	λ (Å)	χ_I (eV)	$\log gf$	EW $_{\odot}$ (mÅ)
Na I - 2 lines				5662.16	2.32	-0.123	23.5	5301.05	1.71	-1.950	19.5
6154.23	2.10	-1.622	36.6	5716.46	2.30	-0.869	5.7	5342.71	4.02	0.606	32.3
6160.75	2.10	-1.363	54.3	5739.48	2.25	-0.781	7.7	5352.05	3.58	0.004	24.4
Mg I - 3 lines				5766.33	3.29	0.326	9.6	5647.24	2.28	-1.594	14.0
5711.09	4.35	-1.777	105.6	5965.84	1.88	-0.492	26.7	6814.95	1.96	-1.822	18.8
6318.71	5.11	-2.046	39.1	5978.55	1.87	-0.602	22.6	Ni I - 54 lines			
6319.24	5.11	-2.300	25.2	6064.63	1.05	-1.941	8.3	4512.99	3.71	-1.467	19.4
Al I - 2 lines				6126.22	1.07	-1.416	22.1	4705.92	3.66	-1.881	9.8
6696.03	3.14	-1.571	36.2	6258.11	1.44	-0.435	51.5	4732.46	4.11	-0.583	42.8
6698.67	3.14	-1.886	21.1	6261.10	1.43	-0.491	49.2	4806.99	3.68	-0.593	61.6
Si I - 13 lines				6599.12	0.90	-2.069	9.3	4912.03	3.77	-0.712	51.8
4947.61	5.08	-2.307	18.3	Ti II - 7 lines				4946.04	3.80	-1.224	26.2
5517.54	5.08	-2.496	12.9	4583.41	1.16	-2.840	31.8	4952.29	3.61	-1.261	32.3
5645.61	4.93	-2.068	35.8	4636.33	1.16	-3.152	19.8	4976.33	1.68	-3.002	37.7
5684.49	4.95	-1.642	61.2	4657.20	1.24	-2.379	49.3	4995.66	3.63	-1.611	17.9
5701.11	4.93	-2.034	37.7	4708.67	1.24	-2.392	48.9	5010.94	3.63	-0.901	48.8
6125.02	5.61	-1.555	31.7	4911.20	3.12	-0.537	52.3	5081.11	3.85	0.064	93.5
6145.02	5.62	-1.425	38.8	5211.54	2.59	-1.490	32.8	5094.41	3.83	-1.108	30.3
6195.46	5.87	-1.666	17.1	5490.70	1.57	-2.800	20.0	5392.33	4.15	-1.354	12.0
6237.33	5.61	-1.116	61.1	V I - 8 lines				5435.86	1.99	-2.432	51.7
6243.82	5.62	-1.331	44.8	5670.85	1.08	-0.482	18.8	5468.11	3.85	-1.641	12.0
6721.85	5.86	-1.156	44.0	5727.05	1.08	-0.015	38.8	5578.73	1.68	-2.649	56.4
6741.63	5.98	-1.625	15.5	6039.73	1.06	-0.747	12.4	5587.87	1.93	-2.479	52.9
6800.60	5.96	-1.787	11.5	6081.45	1.05	-0.692	14.1	5589.36	3.90	-1.148	26.7
Ca I - 12 lines				6090.21	1.08	-0.150	33.5	5625.32	4.09	-0.731	37.8
5261.71	2.52	-0.677	97.7	6119.53	1.06	-0.451	21.6	5641.88	4.11	-1.017	24.1
5349.47	2.71	-0.581	94.6	6243.11	0.30	-1.067	27.8	5643.08	4.16	-1.234	15.1
5512.98	2.93	-0.559	84.8	6251.83	0.29	-1.431	15.0	5694.99	4.09	-0.629	43.1
5867.56	2.93	-1.592	25.1	Cr I - 20 lines				5748.36	1.68	-3.279	28.0
6156.02	2.52	-2.497	9.6	4575.11	3.37	-1.004	10.0	5754.66	1.93	-2.014	75.0
6161.29	2.52	-1.313	60.6	4626.18	0.97	-1.467	83.3	5805.22	4.17	-0.604	40.8
6166.44	2.52	-1.155	69.9	4633.25	3.13	-1.215	10.4	5847.00	1.68	-3.410	23.0
6169.04	2.52	-0.800	92.2	4700.61	2.71	-1.464	14.0	6007.31	1.68	-3.374	24.8
6449.82	2.52	-0.733	98.1	4708.02	3.17	-0.104	55.0	6086.29	4.27	-0.471	43.5
6455.60	2.52	-1.404	56.3	4730.72	3.08	-0.345	46.3	6108.12	1.68	-2.512	65.0
6471.67	2.53	-0.825	91.2	4767.86	3.56	-0.599	16.1	6111.08	4.09	-0.823	34.2
6499.65	2.52	-0.917	85.8	4801.03	3.12	-0.251	49.6	6119.76	4.27	-1.316	10.9
Sc I - 2 lines				4936.34	3.11	-0.343	45.6	6128.98	1.68	-3.368	25.3
4743.82	1.45	0.297	8.0	5122.12	1.03	-3.166	12.9	6130.14	4.27	-0.938	22.1
5671.82	1.45	0.533	14.6	5214.14	3.37	-0.784	16.4	6175.37	4.09	-0.534	49.0
Sc II - 7 lines				5238.97	2.71	-1.427	15.9	6176.82	4.09	-0.266	63.7
4670.41	1.36	-0.507	60.8	5247.57	0.96	-1.618	82.0	6177.25	1.83	-3.538	14.6
5526.82	1.77	0.140	76.3	5287.18	3.44	-0.954	10.4	6186.72	4.11	-0.888	30.5
5657.88	1.51	-0.326	66.9	5348.33	1.00	-1.229	100.1	6191.19	1.68	-2.309	74.8
5667.14	1.50	-1.025	33.9	5480.51	3.45	-0.997	9.5	6204.61	4.09	-1.112	22.0
5684.19	1.51	-0.946	37.2	5781.18	3.32	-0.886	15.5	6223.99	4.11	-0.954	27.7
6245.62	1.51	-1.022	34.9	5783.07	3.32	-0.472	31.4	6230.10	4.11	-1.132	20.6
6604.59	1.36	-1.162	36.3	5787.92	3.32	-0.183	46.0	6322.17	4.15	-1.164	18.4
Ti I - 24 lines				6882.52	3.44	-0.392	32.2	6327.60	1.68	-3.086	38.6
4555.49	0.85	-0.575	63.7	Cr II - 2 lines				6360.81	4.17	-1.145	18.5
4562.63	0.02	-2.718	10.9	4592.05	4.07	-1.252	47.6	6378.26	4.15	-0.830	31.8
4645.19	1.73	-0.666	22.0	5279.88	4.07	-2.006	19.3	6424.86	4.17	-1.372	12.1
4820.41	1.50	-0.429	43.1	Mn I - 5 lines				6532.88	1.93	-3.418	15.8
4913.62	1.87	0.068	50.2	4502.21	2.92	-0.523	57.0	6586.32	1.95	-2.768	41.8
4921.78	2.17	0.183	41.8	4739.11	2.94	-0.462	60.1	6598.60	4.24	-0.914	24.9
4926.15	0.82	-2.214	6.4	4761.51	2.95	-0.147	75.2	6635.13	4.42	-0.779	23.6
5016.17	0.85	-0.657	63.2	5377.62	3.84	-0.068	40.8	6643.63	1.68	-1.994	93.2
5113.44	1.44	-0.861	27.0	6013.49	3.07	0.046	86.2	6767.78	1.83	-2.136	79.2
5145.47	1.46	-0.622	37.0	Co I - 8 lines				6772.32	3.66	-0.963	49.2
5295.78	1.07	-1.677	12.4	4594.63	3.63	-0.279	12.5	6842.04	3.66	-1.496	24.2
5490.16	1.46	-1.008	21.4	4792.86	3.25	-0.080	32.7				
5503.90	2.58	-0.218	12.3	4813.48	3.22	0.177	45.9				

3.4 Spectral Analysis of the Full Sample

We proceeded as in subsection 3.3.7, but this time for the full sample of 451 stars. As we have seen before, the chemical abundances of the elements in study were derived

via a standard Local Thermodynamic Equilibrium (LTE) using a differential analysis relative to the Sun.

First, we used ARES to automatically measure the lines listed in Table 3.2 for every star of the catalogue. The ARES parameters that we used were the same as in subsection 3.3.3 (smoother = 4; space = 2 and lineresol = 0.07) except 'rejt' that changed with the S/N ratio of each star, according to Sousa et al. (2008), and 'miniline' that was set to 2 (to make sure that the weakest lines measured in the spectrum of the Sun were not excluded in the other stars due to some weakening effect in the strength of the lines - an effect typically observed in the hottest stars of this sample).

Then, using the EWs and a grid of ATLAS9 atmospheres (Kurucz 1993) with the corresponding star parameters (effective temperature, surface gravity, microturbulence and metallicity - see Table 3.1) we computed the abundances of the elements with the 'abfind' driver of the 2002 version of MOOG (Snedden 1973). A FORTRAN program was made to coordinate the calculations and set up an organised database of the output data. To account for random events that might 'fall' out of the normal distribution range (cosmic rays, bad pixels, unknown effects), we removed in every star and for every element all the lines with $\Delta A > 2\sigma$ relative to the mean abundance value. Then, a new final mean abundance value was derived. A sample of the final abundance results can be seen in Table 4.1.

3.4.1 Uncertainties

Uncertainties can introduce different errors in the calculated abundances. Random errors can affect individual lines in the calculation of EWs and systematic errors can surface due to blending and NLTE effects or to a poor location of the lines in the continuum. To avoid both types of errors, we should have high quality data and as many lines as possible for each element. Unfortunately we were only able to select 2/3 lines for Mg, Na, Al, CrII and ScI. The lack of statistical data can introduce systematic bias extremely difficult to locate in our results. Therefore, all conclusions regarding these elements should be taken with caution. We have also performed an uniform analysis of the sample. This minimises possible errors due to differences in line lists, atmospheric parameters, oscillator strength biases, applied methodologies, etc.

In the end, the final abundance results had a typical dispersion that ranged from about $rms = 0.02$ dex for aluminium to $rms = 0.1$ dex for vanadium. It's important to note that, in this study, we are not taking into account the uncertainties associated with the stellar parameters or with the atmospheric models.

3.4.2 Testing the Stellar Parameters and Searching for Systematic Effects

In order to verify the used stellar parameters, we tested our results in a variety of ways. First, we calculated the slopes of the abundances as a function of the excitation potential (EP) and as a function of the logarithm of the reduced equivalent width (RW) for Ni. The EP is the minimum amount of energy required to bring an electron from its ground state to a given excited state, and the RW is just the EW divided by the wavelength. The slopes are calculated from the abundances given by MOOG for every spectral line and star. In this way we can verify if the excitation equilibrium that was forced for the Fe I lines on every star and used to obtain the stellar parameters (Santos et al. 2000) is acceptable for other species. We can see an example (star HD1461) in Fig. 3.3. We have chosen niquel because it has a good range of both EP and RW, thus allowing a good determination of the slopes.

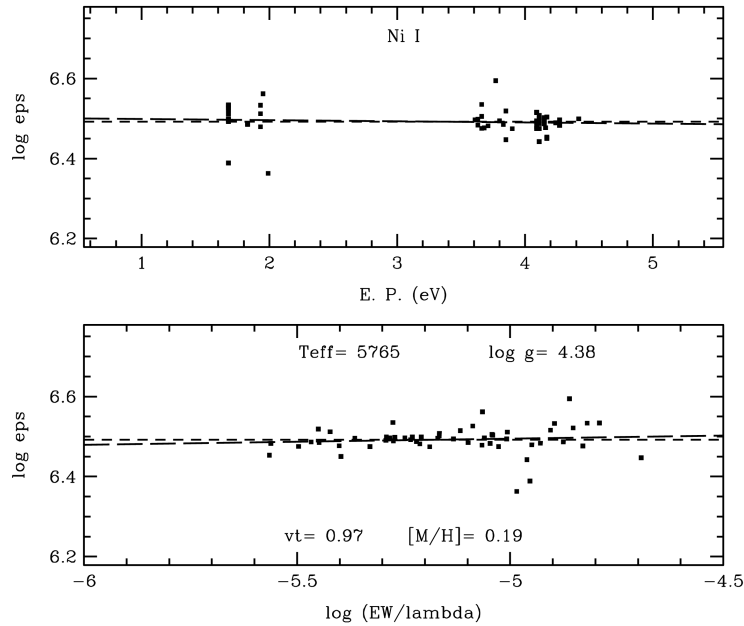


Figure 3.3: Example of the calculation of the slope EP and RW for Ni in the star HD1461. The black squares represent the different spectral lines, the long dashed line the calculated slope and the short dashed line the average value of the abundance (log eps). The slope $EW = -0.010$ and slope $RW = 0.020$.

Then, we plotted the slopes of the EP and RW, obtained for every star, as function of the stellar parameters (T_{eff} , $\log g$, ξ_t and $[\text{Fe}/\text{H}]$), as shown in Figs. 3.4 and 3.5. We expect that the slopes won't change with any of the stellar parameters.

From the analysis of the plots, we can see no discernible trends except in the case of the T_{eff} plots, where we observe that cooler stars have more dispersion on average. This might be due to the fact that it is much more difficult to measure the EW (due

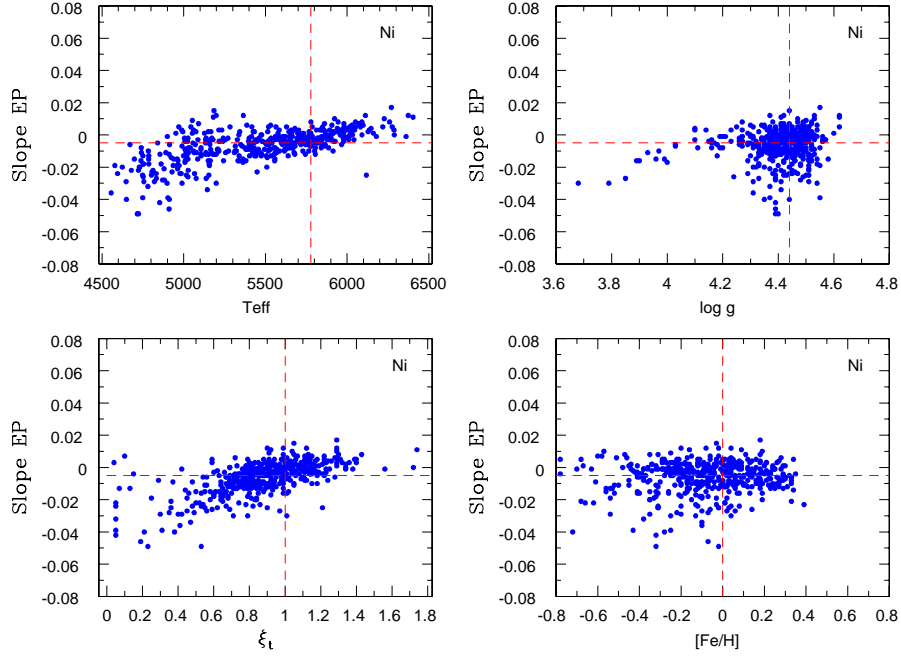


Figure 3.4: Slope EP with T_{eff} , $\log g$, ξ_t and $[Fe/H]$ for Ni. The red dashed lines indicate the solar value.

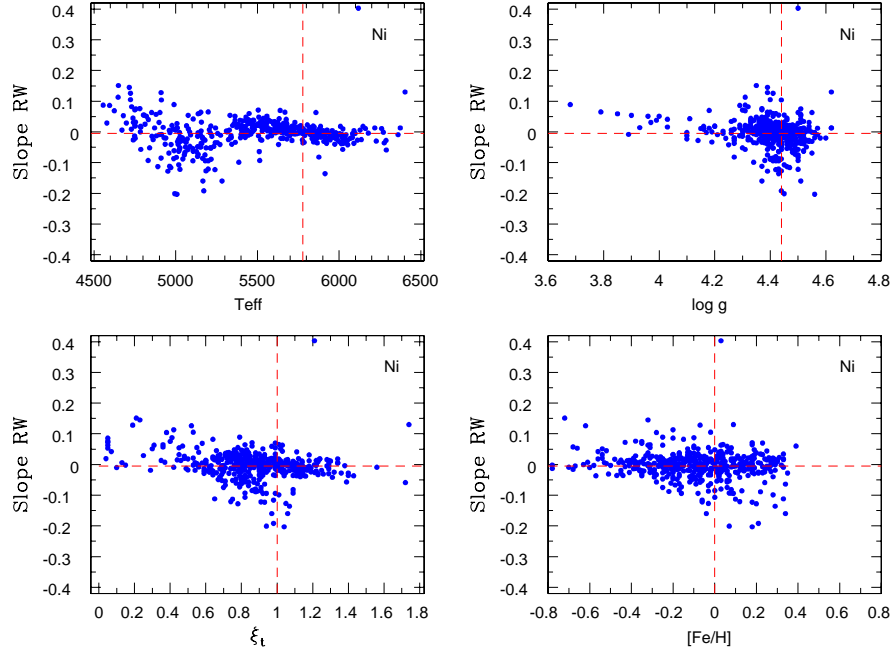


Figure 3.5: Slope RW with T_{eff} , $\log g$, ξ_t and $[Fe/H]$ for Ni. The red dashed lines indicate the solar value.

to blending) in cooler stars. We also observe a slight positive slope in the T_{eff} plot of Fig. 3.5, but it is too small to be relevant. We consider that the observed trends are not very strong, and in general, we consider that for Ni the excitation equilibrium is valid. There is one exception, however: The star HD209458 has a slope RW greater

than 0.4 dex. This can be clearly seen in every plot of Fig. 3.5. The abundance of Ni for this star will be considered invalid and raises serious concerns about the validity of the abundance results for the other elements. Despite that, we will let it appear in the results in order to see how such an error can propagate into the final results.

We have also plotted the $[\text{CrI}/\text{CrII}]$ value with T_{eff} and $\log g$ to ensure that the ionisation equilibrium that was forced to the FeII lines (Santos et al. 2000) was acceptable to chromium (i.e. the abundance of CrII was forced to be equal to the abundance of CrI). This is depicted in Fig. 3.6. We expect that $[\text{CrI}/\text{CrII}]$ will be independent of T_{eff} and $\log g$, with value around zero.

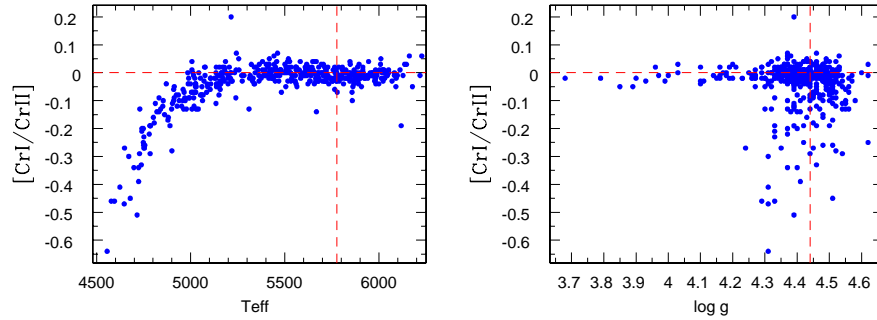


Figure 3.6: Plots of $[\text{CrI}/\text{CrII}]$ with T_{eff} and $\log g$. The red dashed lines indicate the solar value.

However, there is a divergence of the expected ratio for stars with $T_{\text{eff}} < 4900$ K. This result raises many doubts on the abundance values derived for stars with lower temperatures.

Finally, we plotted the abundance of every element as a function of T_{eff} and $\log g$, represented by Figs. 3.7 and 3.8, respectively. We used the $[\text{X}/\text{Fe}]$ ratio to take into account the trend of the galactic chemical evolution. The identification of each element is located at the top right corner of the respective plot. The slopes of $[\text{X}/\text{Fe}]$ with T_{eff} per 1000 K and with the surface gravity are listed in Table 3.3.

Table 3.3: Slopes of $[\text{X}/\text{Fe}]$ ratio with T_{eff} per 1000 K and with $\log g$.

Species	Slope(T) \pm rms	Slope(g) \pm rms	Species	Slope(T) \pm rms	Slope(g) \pm rms
Si	-0.036 ± 0.051	-0.037 ± 0.053	CrI	-0.053 ± 0.026	0.038 ± 0.033
Ca	-0.044 ± 0.069	0.053 ± 0.071	CrII	-0.177 ± 0.084	0.067 ± 0.111
TiI	-0.191 ± 0.084	0.085 ± 0.114	Co	-0.138 ± 0.070	-0.175 ± 0.087
TiII	0.069 ± 0.077	-0.045 ± 0.082	Ni	-0.019 ± 0.035	-0.085 ± 0.034
ScI	-0.369 ± 0.142	0.015 ± 0.208	Na	-0.017 ± 0.066	-0.107 ± 0.066
ScII	0.037 ± 0.061	-0.184 ± 0.059	Mg	-0.033 ± 0.096	-0.052 ± 0.097
Mn	-0.034 ± 0.093	-0.187 ± 0.091	Al	-0.159 ± 0.080	-0.111 ± 0.102
V	-0.452 ± 0.086	0.074 ± 0.204			

We observe significant trends with T_{eff} for TiI, ScI, V, CrII, Co and Al. We can clearly see that the trend away from the expected value, except for Co and Al, is heavily influenced by the cooler stars, where the abundance might have been overestimated

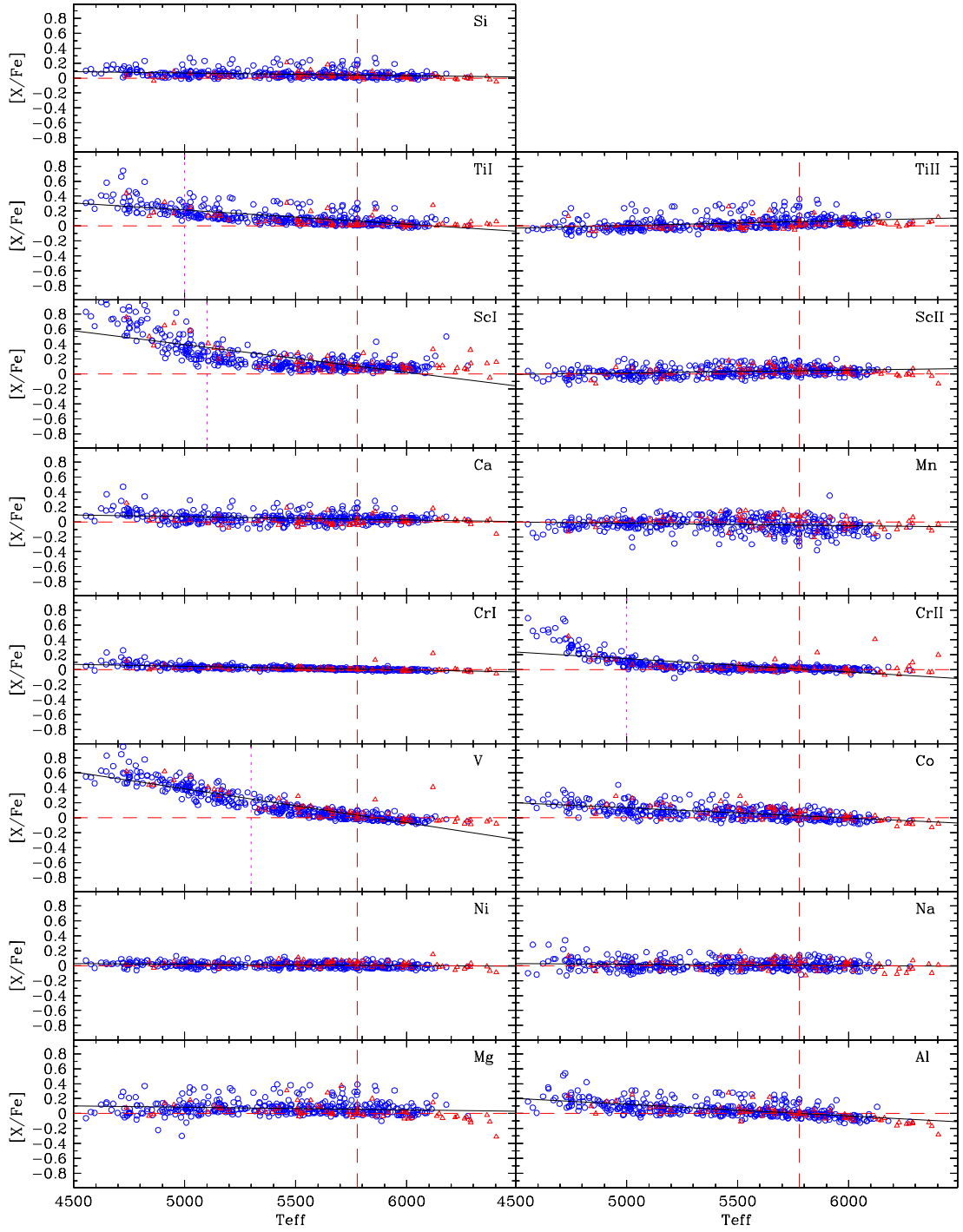


Figure 3.7: $[X/Fe]$ vs. T_{eff} . The red triangles and the blue circles represent the planet host stars and the stars without planetary companions, respectively. The solid black lines represent the linear fits of the data. The red dashed lines indicate the solar value and the magenta vertical dotted lines indicate the cutoff temperature when appropriate.

due to blending effects, to deviations from the excitation or ionisation equilibrium or to problems associated with the differential analysis: we must not forget that the

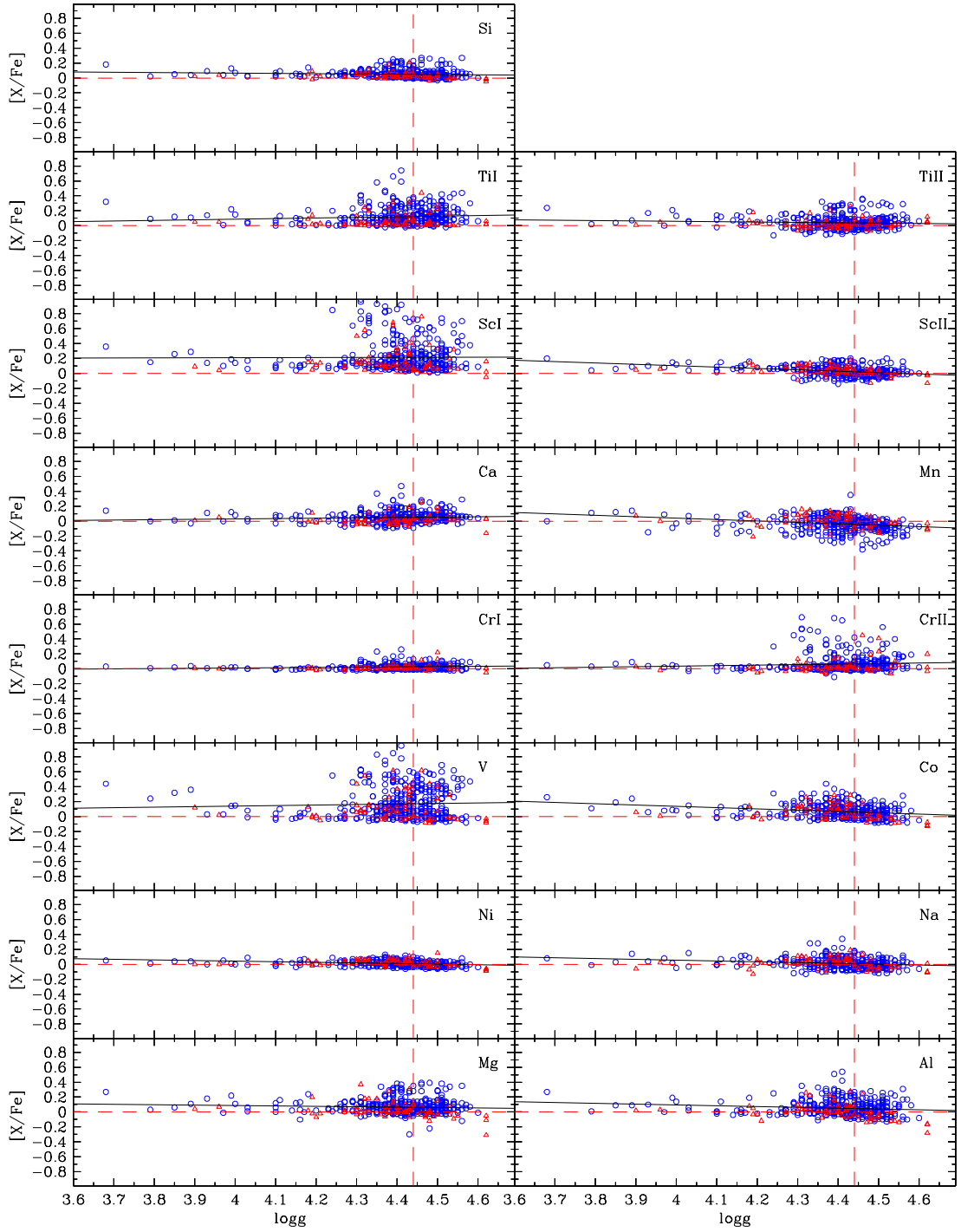


Figure 3.8: $[X/Fe]$ vs. $\log g$. The red triangles and the blue circles represent the planet host stars and the stars without planetary companions, respectively. The solid black lines represent the linear fits of the data. The red dashed lines indicate the solar value.

oscillator strengths were calculated for the Sun.

In order to account for these effects we have decided to establish a cutoff temperature: $T_{cutoff} = 5000$ K for TiI and CrII, $T_{cutoff} = 5100$ K for ScI and $T_{cutoff} = 5300$ K

for V. We shall note this when we analyse the results. We do not know how to explain the observed trends in Co and Al. They might be related to NLTE effects that were not taken into account in this analysis.

In the case of the $\log g$ plots, a clear trend is much more difficult to discern: most stars are in the (4.2 - 4.6) region. Moreover, we verify the existence of a huge dispersion in the same region for ScI, V and CrII. Despite that, we can see decreasing trends in ScII, Mn and Co, but we think that they are not relevant.

Chapter 4

Results: the Abundance of Stars with Planets

The major goal of this study is the determination and comparison of the abundances between two groups of stars: stars with planets and stars without planets. As we have seen in the previous chapter, we have a catalogue with 451 stars, from which 66 stars host planetary companions. We hope that this smaller sample will be enough to verify if there are any peculiarities that might differentiate planet host and non-planet host stars. In this chapter, we will see what we have found. We will present the results obtained for the abundances of the stars and compare them with similar studies from the literature.

A sample of the results are presented in Table 4.1. The complete results are available online (in .rdb format) at http://www.astro.up.pt/~nuno/vasco_table4.1.tar.gz.

Table 4.1: Sample table of the derived abundances of the species, rms and number of lines (n) for each star.

Star ID	[Si/H]	rms	n	[Ca/H]	rms	n	[ScI/H]	rms	n	[ScII/H]	rms	n	...
...
HD117105	-0.21	0.02	12	-0.19	0.03	11	-0.14	0.05	2	-0.20	0.04	7	...
HD117207	0.24	0.05	12	0.18	0.02	11	0.27	0.03	2	0.22	0.08	7	...
HD117618	0.05	0.02	13	0.05	0.03	11	0.09	0.01	2	0.06	0.04	7	...
HD119638	-0.11	0.02	13	-0.09	0.03	11	-0.06	0.01	2	-0.13	0.03	7	...
HD119782	-0.03	0.04	13	0.01	0.09	11	0.09	0.04	2	-0.06	0.02	6	...
HD121504	0.12	0.02	13	0.15	0.03	11	0.20	0.01	2	0.13	0.04	7	...
HD122862	-0.08	0.01	12	-0.06	0.04	12	-0.02	0.01	2	-0.06	0.04	7	...
HD123265	0.27	0.08	13	0.16	0.06	12	0.44	0	2	0.29	0.09	7	...
...

4.1 Comparison of [X/H] Values with the Literature

In order to test the reliability of our results, we made a comparison of the derived abundances with the ones obtained by Bodaghee et al. (2003), Beirão et al. (2005) and

4.1. COMPARISON OF $[X/H]$ VALUES WITH THE LITERATURE

Gilli et al. (2006) (hereafter BOD, BEI and GIL respectively), as seen in Fig. 4.1.

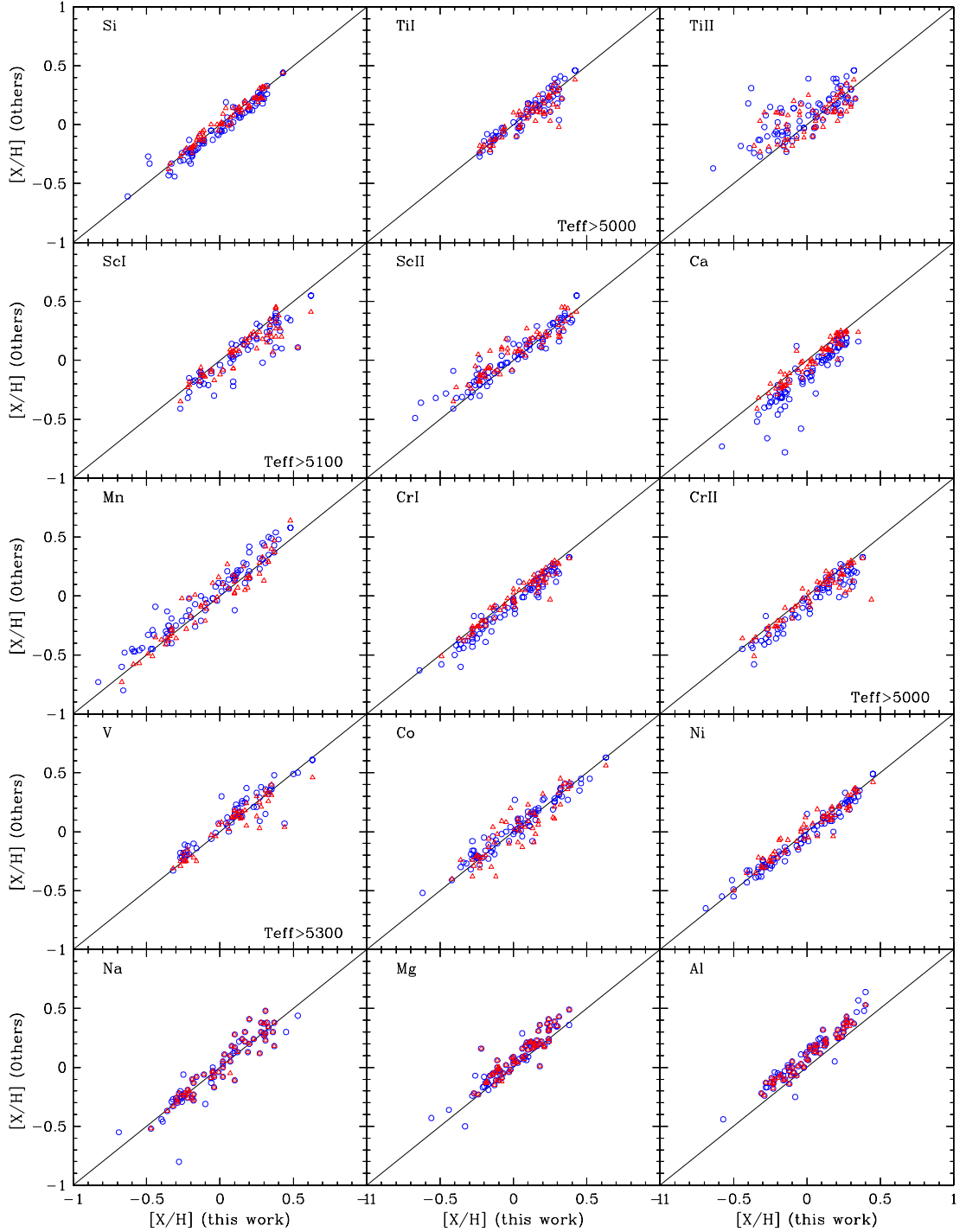


Figure 4.1: Comparison of the derived abundances with other authors: Gilli et al. (2006) (blue circles), Bodaghee et al. (2003) (red triangles, except for Na, Mg and Al) and Beirão et al. (2005) (red triangles for Na, Mg and Al). The elements are identified at the top left corner of each plot.

All common stars were used except for TiI, ScI, CrII and V, where we only used stars above a cutoff effective temperature, as it was determined in subsection 3.4.2.

We must note that, for Na, Mg and Al, most of GIL results are equal to BEI, simply because GIL used BEI results.

We can see that, in general terms, our results agree with the $[X/H]$ obtained by the other authors. However, we observe a slight systematic overabundance trend in Ca, CrI and CrII (GIL) and a slight systematic underabundance in Mg and Al (GIL and BEI). It's worth mentioning the extra underabundance of a few stars in V and Ca. We do not know the origin of these differences. We consider that the observed differences are relatively small and do not compromise the results or the main goal of this work, since we will be doing a differential analysis comparing stars with and without planets.

4.2 The $[X/H]$ Distributions

The distributions of $[X/H]$ of planet hosts and non-planet hosts are depicted in Fig. 4.2. The stars with and without planets are represented by a solid red line and by a dotted blue line, respectively. The blue and red vertical lines above each histogram represent the mean value of metallicity of the non-host planet and the host planet distributions, respectively. Each plot has the name of the respective element in the upper right corner and the cutoff temperature, if appropriate.

We can clearly observe that there is a metallicity excess for planet host stars for all the elements studied. These results are in good agreement with previous similar studies (BOD, BEI and GIL). Our results also agree with previous studies of iron abundances (see section 1.8.1), as expected.

Table 4.2: Average abundance values for stars with and without planets, along with their rms and the difference between the two groups.

Species (X)	Planet hosts		Non-planet hosts		Difference of Averages
	$\langle[X/H]\rangle$	rms	$\langle[X/H]\rangle$	rms	
Si	0.12	0.17	-0.06	0.21	0.18
TiI	0.16	0.14	0.00	0.18	0.17
TiII	0.11	0.15	-0.08	0.20	0.19
ScI	0.24	0.19	0.04	0.23	0.20
ScII	0.12	0.20	-0.09	0.24	0.21
Ca	0.11	0.14	-0.06	0.18	0.17
Mn	0.09	0.25	-0.16	0.31	0.25
CrI	0.10	0.17	-0.09	0.22	0.20
CrII	0.13	0.18	-0.07	0.22	0.20
V	0.16	0.20	-0.03	0.25	0.19
Co	0.15	0.21	-0.05	0.26	0.20
Ni	0.11	0.20	-0.11	0.25	0.22
Na	0.10	0.20	-0.11	0.24	0.21
Mg	0.12	0.16	-0.04	0.19	0.16
Al	0.10	0.17	-0.06	0.21	0.16

Table ?? lists the average values of $[X/H]$ along with their rms and the difference of averages between stars with and without planets. These differences go from 0.16 for Mg and Al to 0.25 for Mn. The difference of the average abundance between the two

groups of stars is, on average, slightly below the figures of BOD and GIL by ~ 0.03 dex. The dispersion of this difference is also smaller, likely atesting the quality of our values.

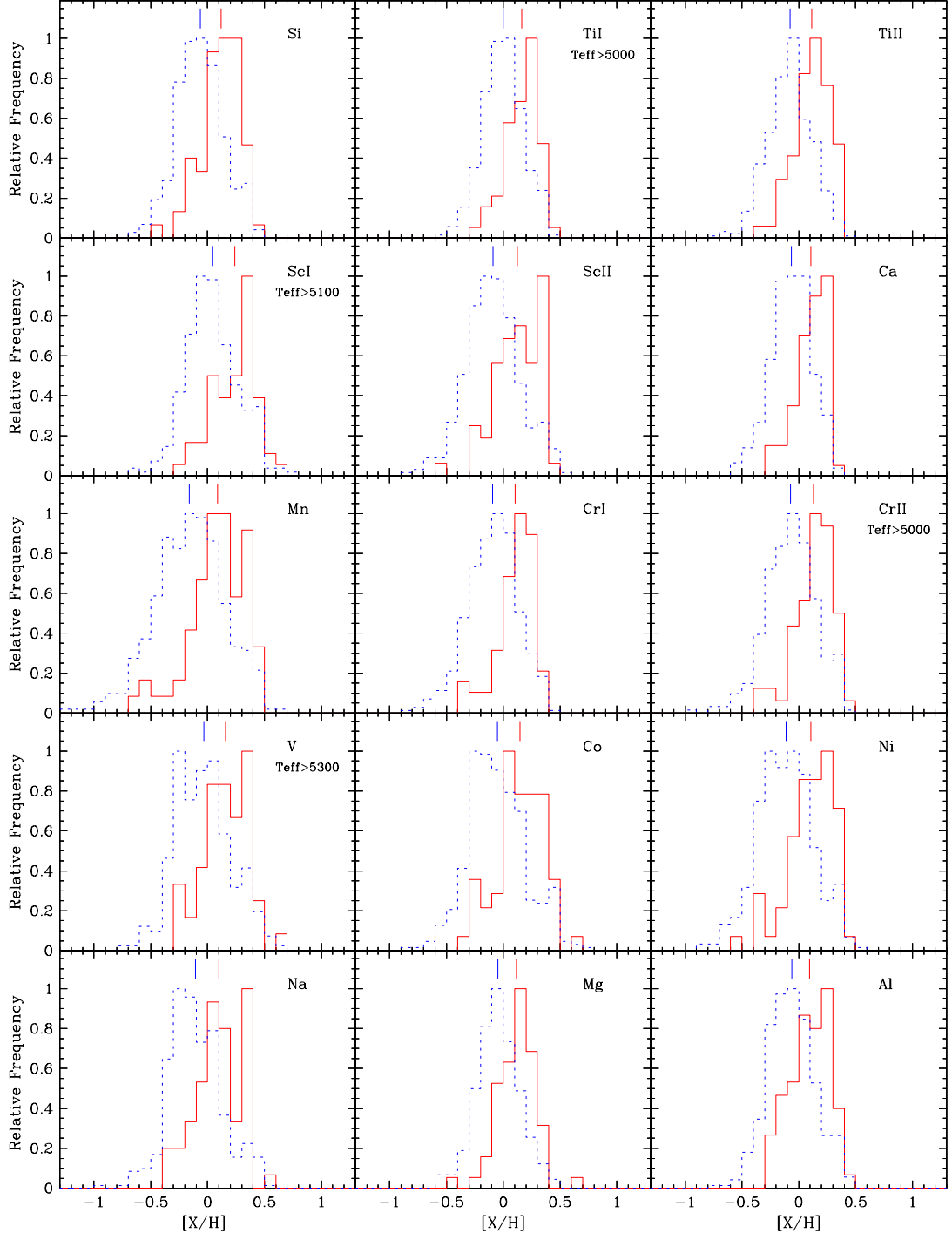


Figure 4.2: $[X/H]$ distribution of the species. The stars with planets and those without them are represented by a solid red line and by a blue dotted line respectively. The mean value is pictured by a red (with planets) and blue (without planets) vertical lines above each distribution.

It is interesting to see that in most histograms (except for Mg) the distributions of the abundances in planet host stars are not symmetrical: there is an increase of [X/H] up to a maximum and shortly after there is a huge cutoff in distribution. This cutoff is located at [X/H] \sim 0.4 for TiII, Ca, CrI and Na, [X/H] \sim 0.5 for Si, TiI, ScII, Mn, CrII, V, Co, Ni and Al and [X/H] \sim 0.7 for ScI. The cutoff might suggest that we are looking at the metallicity limit of the solar neighbourhood stars (e.g. Santos et al. 2003), as most of the planet hosts are at the high metallicity end of the sample.

Some histograms seem to be slightly bimodal (Mn, V, Na). We do not know why this happens. It might be due only to small number statistics.

4.3 The [X/Fe] versus [Fe/H] Plots

The [X/Fe] vs. [Fe/H] plots are traditionally used to study the chemical evolution of the galaxy as well as to identify the stars of the different populations of the galaxy (thin disk, thick disk, halo), which have distinct abundance ratios (see e.g. Bensby et al. 2003, Fuhrmann 2004). In our study, we will analyse them only to observe if there are any differences in the abundance of stars with and without planets for a similar value of [Fe/H]. A chemical evolution study will be postponed to the near future: we refer the prospective reader to McWilliam (1997). The [Fe/H] can be used as a time variable, but this is still controversial.

The abundance value of the X element relative to the Fe abundance of each star is calculated by subtracting the derived abundance of the X element of a star with the [Fe/H] values (provided by Sousa et al. 2008) of the same star. Therefore, $[X/Fe] = [X/H] - [Fe/H]$.

Fig. 4.3 illustrate the plots of the studied species abundance relative to iron with [Fe/H]. The blue circles and the red triangles represent the stars with and without planets, respectively. The red dashed lines target the solar value. The identification of each element is located in the upper right corner of the respective plot. The cutoff temperature is indicated when appropriate. The black circle, cross, square and star correspond to HD209458, HD147513, HD66428 and HD142, respectively. These four stars will be analysed separately in subsection 4.3.1.

We also did the same [X/Fe] vs. [Fe/H] plots only for stars with $T_{eff} = T_{\odot} \pm 200$ K (Fig. 4.4). These plots allow us to have a more accurate picture of the trends and differences among the two groups of stars: in a differential analysis like this one, the closer the star temperature is to the solar temperature, the more accurate, in average, the derived abundance is. We hope that these latter figures help to uncover some hidden trend or a particular trend related to solar type stars, as they have much less

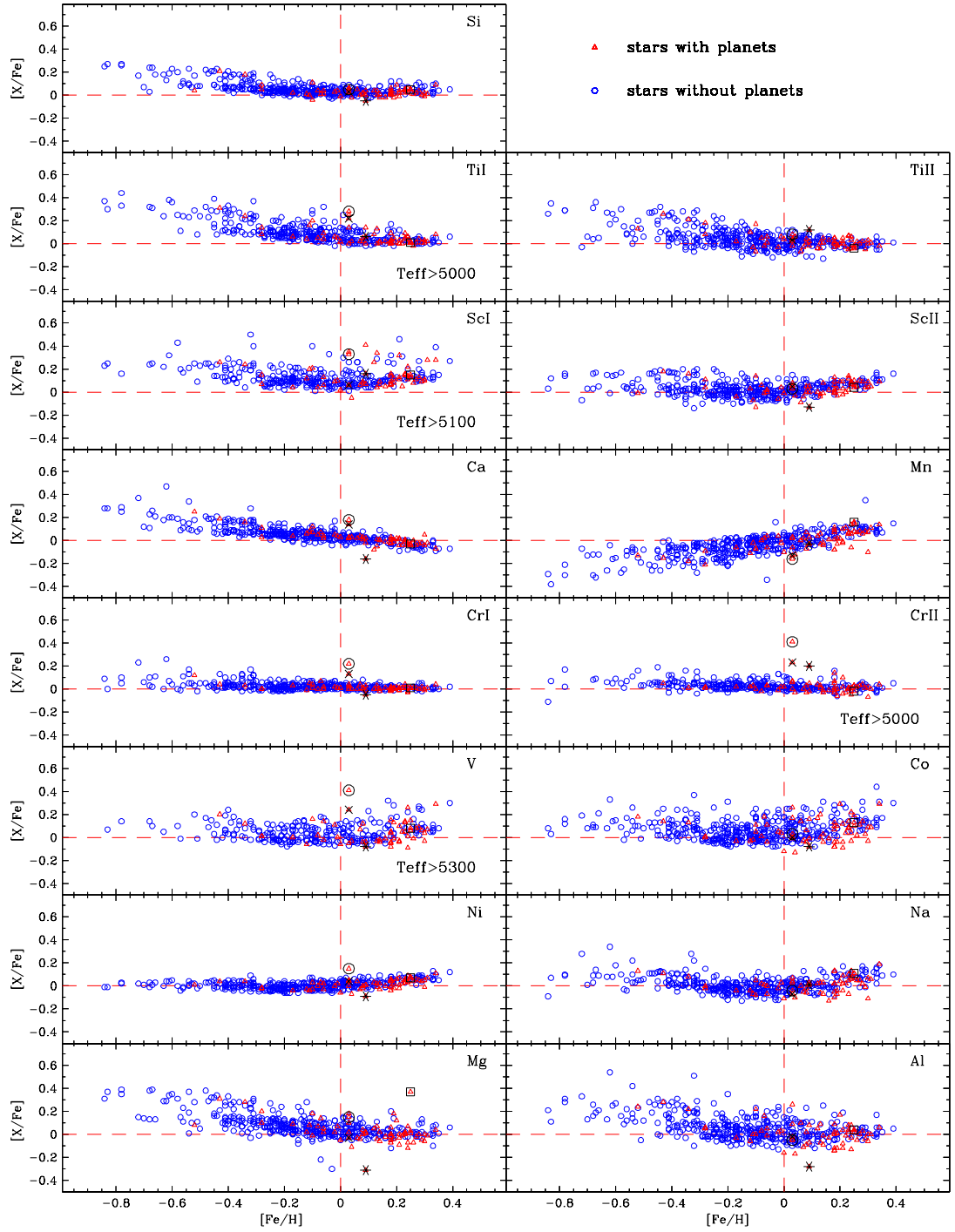


Figure 4.3: $[X/Fe]$ vs. $[Fe/H]$ plots of the elements in study. The red triangles and the blue circles represent the stars with and without planets respectively. The intersection of the dashed red lines indicate the solar value. Each element is identified in the upper right corner of the respective plot and the cutoff temperature is indicated in the lower right corner when appropriate. The black circle, cross, square and star correspond to HD209458, HD147513, HD66428 and HD142, respectively.

scatter than the ones in Fig. 4.3.

We did not found any differences between the stars with and without planets for

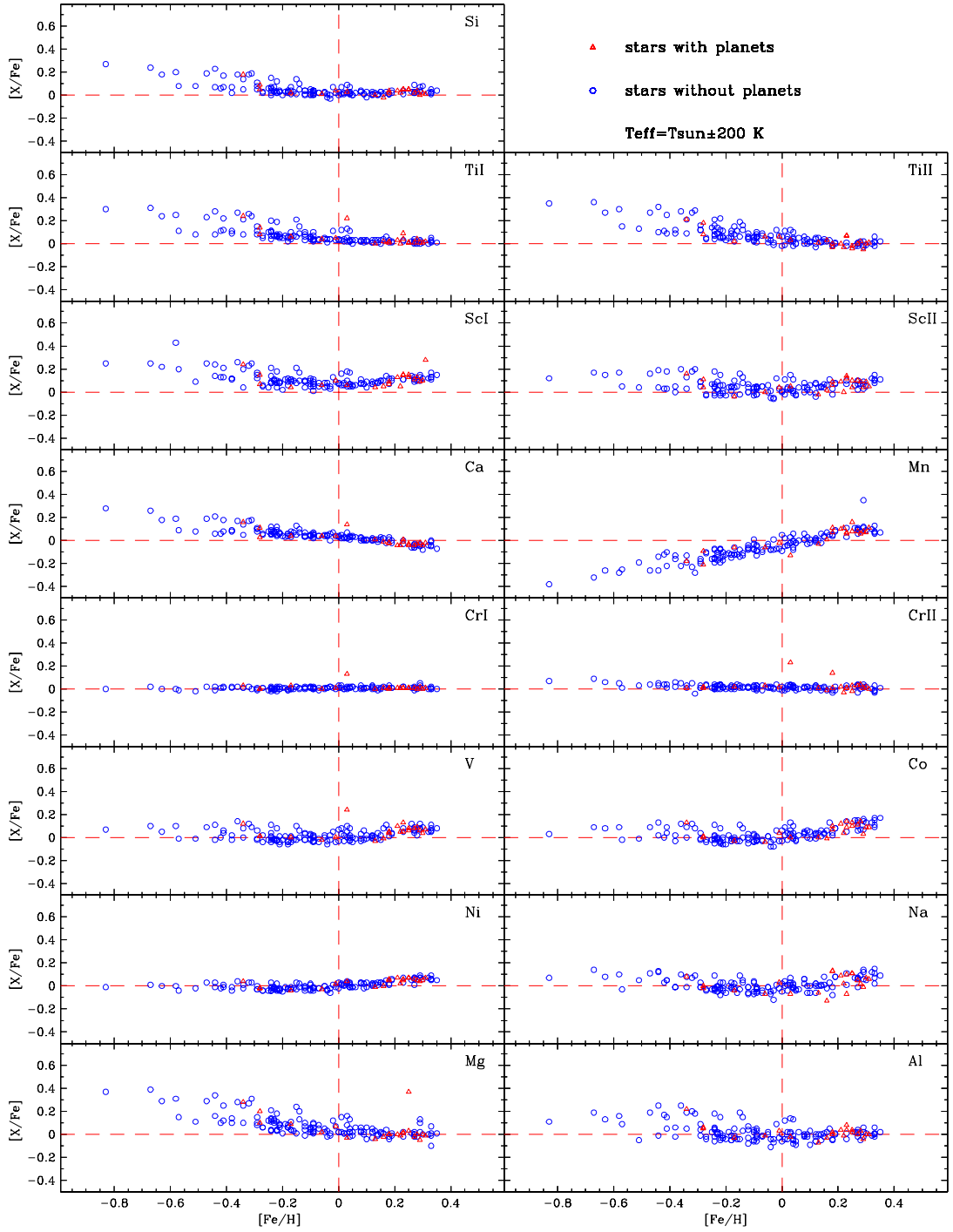


Figure 4.4: $[X/Fe]$ vs. $[Fe/H]$ plots of the elements in study for $T_{eff} = T_{\odot} \pm 200$ K. The red triangles and the blue circles represent the stars with and without planets respectively. The intersection of the dashed red lines indicate the solar value. Each element is identified in the upper right corner of the respective plot.

a given $[Fe/H]$ value. The exceptions are restricted to the isolated cases described in subsection 4.3.1. The results agree in general with previous similar studies like, for instance, Gonzalez et al. (2001), Takeda et al. (2001), Sadakane et al. (2002), Bodaghee

et al. (2003), Beirão et al. (2005), Fischer & Valenti (2005) and Gilli et al. (2006). This gives us confidence in our results. The reported cases of potential trends described by other authors like, for instance, Sadakane et al. (2002) for vanadium, Bodaghee et al. (2003) for V, Mn, Co and Ti, Gilli et al. (2006) for V, Co, Mg and Al and Robinson et al. (2006) for Si and Ni were not found.

We have also identified what seems to be a smaller group of stars that has a systematic average overabundance of ~ 0.1 0.2 dex and spans from [Fe/H] values of -0.85 to -0.1 dex in the Fig. 4.3 plots of Si, TiI, ScII and Mg. This feature becomes even clearer in Fig. 4.4. The group might be a different population of stars, originating from the thick disk of the galaxy (e.g. Bensby et al. 2003; Fuhrmann 2004). This will be the object of further investigation in a future work. We will not pursue this matter for now.

4.3.1 Metallicity Anomalies in Planet Host Stars

In our analysis we have found some planet host stars with unusual high or low values of abundance when compared to stars with similar [Fe/H]. We will analyse each case in a different paragraph.

The star HD209458 has very high overabundance values when compared to stars with similar [Fe/H]. This can be observed in Fig. 4.3 on the plots of TiI, Ca, CrI, V ($\approx +0.3$ dex) and Ni ($\approx +0.15$ dex). However, this star has a RW slope greater than 0.4 dex for Ni and, therefore, the derived abundance values might be incorrect (see subsection 3.4.2). Consequently, we cannot conclude anything.

The overabundance values observed in HD147513 are very similar to the ones of HD209458 but they are somewhat lower for the same plots except Ni, in which it has a normal abundance value. Nevertheless, it remains isolated from other stars of similar [Fe/H]. The value of [Mn/Fe] is also lower than the average value at the same [Fe/H]. We didn't find any bias for this star.

The huge overabundance value of HD66428 (≈ 0.4 dex) in the MgI plot is a mystery. This star has normal values for every other element. However, the abundance of MgI has a huge dispersion ($\text{rms} = 0.46$ dex). This means that we cannot conclude anything. Despite that, we have not found any bias for this star.

The star HD142 is a very interesting case: it has a very high underabundance in the plots of Mg, Al (≈ -0.3 dex), Ca (≈ -0.2 dex) and a slight underabundance in Si, ScII, Mn, CrI, V, Co and Ni. Curiously, it has a very slight overabundance in TiI and TiII. CrII has a high overabundance value: this implies that the result for chromium is not conclusive - we have two contradictory values for the same element. The slope RW for Ni has a reasonably high value of 0.13 (see subsection 3.4.2). Therefore, the

underabundance results for this star are inconclusive. Due to the high temperature of this star ($T_{eff} = 6403$ K), the abundance analysis of this star might suffer from NLTE effects, which might explain the oscillation of the abundance values.

We have not found any abundance anomalies in the stars previously described in the literature: the underabundance of Ca in HD209100 derived by Bodaghee et al. (2003) was found to be well within the rms values for that element and the overabundance of Mg and Al in the host star HD168746 described by Sadakane et al. (2002), Laws et al. (2003) and Gilli et al. (2006) was not found. In a limited search through the literature we have not seen any reference to the stars with abundance anomalies found in the present study.

Chapter 5

Conclusions and Future Work

We have derived the abundances of 12 elements (silicon, calcium, titanium, scandium, manganese, chromium, vanadium, cobalt, nickel, sodium, magnesium and aluminium) in a detailed and homogeneous spectral analysis from a catalogue of 451 stars of the HARPS 'high precision' GTO planet search program, from which 66 planets are known to harbour planetary companions. Comparison studies with other authors were made to assure the consistency of our results. The $[X/H]$ distributions as well as the plots of $[X/Fe]$ vs. $[Fe/H]$ were analysed to compare the trends of stars with and without planets.

5.1 Conclusions

Our concluding remarks are as follows:

- We derived abundance values with an high precision and low dispersion. However, we must take the results for Co and Al with some reservations: the derived abundances have a non-negligible bias with T_{eff} , as seen in subsection 3.4.2. We consider that the removal of the cooler stars in the analysis of TiI, ScI, CrII and V did not affect the final results.
- We confirm that there is an overabundance of metallicity in planet host stars, common to all species, as expected from the results in previous works. The results suggest that the efficiency of planetary formation correlates strongly with the metal content of the host star: the probability of finding a star with giant planets is greater in stars with a high $[X/H]$. This has implications on the models of planetary formation: the results favour the core accretion model and might help constrain the formation conditions of planetary bodies.

- We did not find any different trends in the $[X/Fe]$ vs. $[Fe/H]$ plots between stars with and without planets, in agreement with previous studies. The stars that harbour planetary companions simply seem to be in the high metallicity tail of the distribution, following the same trends as the stars without planets. This might favour the primordial origin as the preferred cause for the observed high metallicities in planet host stars.
- We found only one case where the pollution scenario might be important (see section 1.7): HD147513 has an overabundance in some species and no bias has been found. This particular case needs to be investigated in a future work. The analysis of HD142, HD66428 and HD209458 is inconclusive.

5.2 Future Work

In the future we hope to continue our work in the following directions:

- Investigate the galactic chemical evolution of the studied elements. This can lead to a better understanding on the different origins of the elements and their trends with metallicity (and with time).
- Extend the abundance study to the volatile elements and investigate the trends of abundance with the condensation temperature of the species. This will allow a study on differential accretion, where we could see if some elements are more abundant than others. The outcome of this analysis might favour one of the two hypothesis for the observed anomalous metallicity in planet host stars: the primordial origin or the external pollution process (see section 1.8.2).
- Investigate the relation of metallicity with the orbital parameters (eccentricity, orbital period) and minimum masses of the planetary bodies.
- Confirm and investigate the stars with abundance anomalies discussed in subsection 4.3.1.
- Explore the possibility of the existence and origin of a different star population with higher metallicity in the region of $[Fe/H] < 0$ that appear more clearly in the $[X/Fe]$ vs. $[Fe/H]$ plots of some species (e.g. Si, TiI, ScII, Mg). We speculate that this population might originate from the thick disk of the galaxy and we would like to explore this possibility doing a kinematic analysis on the stars of the sample to confirm that hypothesis.

Bibliography

- Alibert, Y., Baraffe, I., Benz, W., et al. 2006, *A&A*, 455, L25
- Anders, E. & Grevesse, N. 1989, *Geochimica et Cosmochimica Acta*, 53, 197
- Beaulieu, J.-P., Bennett, D. P., Fouqué, P., et al. 2006, *Nature*, 439, 437
- Beirão, P., Santos, N. C., Israelian, G., & Mayor, M. 2005, *ArXiv Astrophysics e-prints*
- Benedict, G. F., McArthur, B. E., Forveille, T., et al. 2002, *ApJ*, 581, L115
- Bennett, D. P., Bond, I. A., Udalski, A., et al. 2008, *ArXiv e-prints*, 806
- Bensby, T., Feltzing, S., & Lundström, I. 2003, *A&A*, 410, 527
- Bodaghee, A., Santos, N. C., Israelian, G., & Mayor, M. 2003, *A&A*, 404, 715
- Boss, A. P. 1997, *Science*, 276, 1836
- Boss, A. P. 2002, *ApJ*, 567, L149
- Charbonneau, D., Brown, T., Latham, D., & Mayor, M. 2000, *ApJ*, 529, L45
- Ecuvillon, A., Israelian, G., Santos, N. C., Mayor, M., & Gilli, G. 2006, *A&A*, 449, 809
- Ecuvillon, A., Israelian, G., Santos, N. C., et al. 2004, *A&A*, 426, 619
- Fischer, D. A., Marcy, G. W., Butler, R. P., et al. 2008, *ApJ*, 675, 790
- Fischer, D. A. & Valenti, J. 2005, *ApJ*, 622, 1102
- Fuhrmann, K. 2004, *Astronomische Nachrichten*, 325, 3
- Gilli, G., Israelian, G., Ecuvillon, A., Santos, N. C., & Mayor, M. 2006, *A&A*, 449, 723
- Gonzalez, G. 1998, *A&A*, 334, 221
- Gonzalez, G., Laws, C., Tyagi, S., & Reddy, B. E. 2001, *AJ*, 121, 432

- Gray, D. F. 2005, *The Observation and Analysis of Stellar Photospheres* (The Observation and Analysis of Stellar Photospheres, 3rd Edition, by D.F. Gray. ISBN 0521851866. Cambridge, UK: Cambridge University Press, 2005.)
- Ida, S. & Lin, D. N. C. 2004a, *ApJ*, 604, 388
- Ida, S. & Lin, D. N. C. 2004b, *ApJ*, 616, 567
- Israelian, G., Santos, N. C., Mayor, M., & Rebolo, R. 2003, *A&A*, 405, 753
- Kupka, F., Piskunov, N., Ryabchikova, T. A., Stempels, H. C., & Weiss, W. W. 1999, *A&AS*, 138, 119
- Kurucz, R. 1993, *ATLAS9 Stellar Atmosphere Programs and 2 km/s grid*. Kurucz CD-ROM No. 13. Cambridge, Mass.: Smithsonian Astrophysical Observatory, 1993., 13
- Kurucz, R. L., Furenlid, I., & Brault, J. T. L. 1984, *Solar flux atlas from 296 to 1300 nm* (National Solar Observatory Atlas, Sunspot, New Mexico: National Solar Observatory, 1984)
- Laws, C. & Gonzalez, G. 2001, *ApJ*, 553, 405
- Laws, C., Gonzalez, G., Walker, K. M., et al. 2003, *AJ*, 125, 2664
- Lovis, C., Pepe, F., Bouchy, F., et al. 2006, in *Presented at the Society of Photo-Optical Instrumentation Engineers (SPIE) Conference*, Vol. 6269, *Ground-based and Airborne Instrumentation for Astronomy*. Edited by McLean, Ian S.; Iye, Masanori. *Proceedings of the SPIE*, Volume 6269, pp. 62690P (2006).
- Marcy, G. W. & Butler, R. P. 1996, *ApJ*, 464, L147+
- Mayor, M., Pepe, F., Queloz, D., et al. 2003, *The Messenger*, 114, 20
- Mayor, M. & Queloz, D. 1995, *Nature*, 378, 355
- McWilliam, A. 1997, *A&A*, 35, 503
- Perryman, M., Hainaut, O., Dravins, D., et al. 2005, *ESA-ESO Working Group on "Extra-solar Planets"*, Tech. rep.
- Pollack, J., Hubickyj, O., Bodenheimer, P., et al. 1996, *Icarus*, 124, 62
- Robinson, S. E., Laughlin, G., Bodenheimer, P., & Fischer, D. 2006, *ApJ*, 643, 484

- Sadakane, K., Ohkubo, M., Takeda, Y., et al. 2002, PASJ, 54, 911
- Sandquist, E. L., Dokter, J. J., Lin, D. N. C., & Mardling, R. A. 2002, ApJ, 572, 1012
- Santos, N. C. 2008, New Astronomy Reviews, 52, 154
- Santos, N. C., Israelian, G., & Mayor, M. 2000, A&A, 363, 228
- Santos, N. C., Israelian, G., & Mayor, M. 2001a, ArXiv Astrophysics e-prints
- Santos, N. C., Israelian, G., & Mayor, M. 2001b, A&A, 373, 1019
- Santos, N. C., Israelian, G., & Mayor, M. 2004, A&A, 415, 1153
- Santos, N. C., Israelian, G., Mayor, M., et al. 2005, A&A, 437, 1127
- Santos, N. C., Israelian, G., Mayor, M., Rebolo, R., & Udry, S. 2003, A&A, 398, 363
- Snedden, C. 1973, Ph.D. Thesis, Univ. of Texas
- Sousa, S. G., Santos, N. C., Israelian, G., Mayor, M., & Monteiro, M. J. P. F. G. 2007, A&A, in press
- Sousa, S. G., Santos, N. C., Mayor, M., et al. 2008, ArXiv e-prints, 805
- Struve, O. 1952, The Observatory, 72, 199
- Takeda, Y., Sato, B., Kambe, E., et al. 2001, PASJ, 53, 1211
- Trilling, D., Benz, W., Guillot, T., et al. 1998, ApJ, 500, 428
- Udry, S., Mayor, M., Benz, W., et al. 2006, A&A, 447, 361
- Udry, S., Mayor, M., Naef, D., et al. 2000, A&A, 356, 590
- Udry, S. & Santos, N. 2007, ARAA, 45, 397
- Vauclair, S. 2004, ApJ, 605, 874